Effects of Upstream Wake Phasing on the Performance of Transonic Compressors

by

Sean Patrick Rock Nolan

S.B., Aeronautics and Astronautics, Massachusetts Institute of Technology, 2003
S.M., Aeronautics and Astronautics, Massachusetts Institute of Technology, 2005

Submitted to the department of Aeronautics and Astronautics in Partial Fulfillment of the Requirements for the Degree of

Doctor of Philosophy in Aeronautics and Astronautics

at the

Massachusetts Institute of Technology

March 2009

[JUNE]

Author: _____
Department of Aeronautics and Astronautics
March 11, 2009

Certified by: _____
Choon S. Tan
Senior Research Engineer
Thesis Supervisor

Certified by: _____
John J. Adamczyk
Senior Technical Specialist, NASA (ret.)
Thesis Supervisor

Certified by: _____
Edward M. Greitzer
H.N. Slater Professor of Aeronautics and Astronautics
Thesis Supervisor

Certified by: _____
Mark Drela
Terry J. Kohler Professor of Fluid Dynamics
Thesis Supervisor

Accepted by: _____
David L. Darmofal
Associate Department Head
Chair, Committee on Graduate Students

Acknowledgements

There are myriad people to thank for their support and contributions in helping this reasearch project reach completion. My primary advisors Prof. Greitzer, Dr. Tan, and Dr. Adamczyk are all greatly appreciated. In addition to being technically proficient and helpful in my growth as an engineer, this trio has an excellent sense of humor, so there was never a dull moment. I am in debt to Prof. Drela, who is also a member of my thesis committee, and his encyclopedic knowledge of boundary layer flows. Prof. Gorrell of BYU imparted his knowledge of blade row interactions to me and helped me immensely throughout the project. Prof. Harris was a great source of support, too. The advice given by Dr. J.P. Chen of Ohio State University and Dr. N. A. Cumpsty of Imperial College is also greatly appreciated.

I am indebted to the members of the Fans and Compressors branch of the Air Force Research Laboratory. Dr. Steven Puterbaugh, David Car, Tom McCray, Michael List, Dr. Shad Reed, Dr. Todd Bailie, Dr. Greg Bloch, Grant Hile, and Curtis Wilson have supported me immensely. Dr. Douglas Rabe of the Compressor Research Facility was a key mentor, as well.

A large portion of the credit for this work also goes to Prof. John-Paul Barrington Clarke and Dr. Seymour Douglas, who mentored me throughout the grad school experience. The advice of James Brooks is also appreciated. There are many others who offered a high standard to strive for and the support to reach that standard, including Coach Halston Taylor, Michael Mallory, Vanessa Evans, and the entire Ron Brown scholar program.

Thanks to Barbara Botros, with whom I worked on this project. Botros offered the idea which eventually blossomed into my thesis work, and for that I am very appreciative, although her friendship is appreciated more. I thank my office mates over the years: Nayden Kambouchev, Alfonso Daniel Villanueva Villareal, Francois LeFloch, Isabelle Delefortrie, and Stevan Jovanovic. Thanks to my other fellow GTL students, including Dave Tarr, Justin Jaworski, Caitlin Smythe, Darius Mobed, Bjoern Benneke, Andreas Peters, George Kiwada, Tom Walker, Sho Sato, Jeff Defoe, Ryan Tam, Georg Reichstein, Shinji Tanaka, Tanya Cruz Garza and Patrick Freuler.

Many thanks to the administrative staff of GTL who provide an environment where work can get done, in spite of the chaos created by the faculty and students. Lori Martinez, Holly Anderson, Diana Park, and Jimmy Letendre were vital to the completion of this research work. Other administrators in the department, including Marie Stuppard, Barbara Lechner, and Robin Palazzolo were also key in completing this work.

My friends I have met in the Northeast helped to keep me balanced. To Michael Razo, Leilani Roser, Shawn Tsosie, Debra Horng, Katie Carbonari, Ricardo Mottley, David Crow, Irene Robles, Natalie Paul, Benjamin Schmeckpeper, Kathryn Schulte, and Craig Wildman, your friendship is much appreciated. Thanks also to Dr. Steven Kleiner, who helped me keep things in proper perspective during some of the rougher spots of the

research project.

I had many friends in the Midwest outside of work that made me feel at home, even though I spent a relatively short time in Dayton, Ohio. Ashley Hawkes, Darius Sanders, Charles Kennedy, Dr. Darnell Diggs, Dr. Eric Jones, David Fortson, Marcia Webster, Alicia Jordan, and the Teague family (Marita, Zedric, Noah, Josh, and Zach) were great sources of support. The friendship of Ashley Ruef, and Josh and Heather Masters was also important to me during the writing of this thesis.

The encouragement and support of my Mum, Janice M. Rock-Nolan, and my brother, Ryan S. R. Nolan, were the most crucial aspects to my being able to complete the graduate program. My dad, Patrick Nolan, has also given useful advice along the way. Additional encouragement was given by my grandparents, aunts, uncles, and cousins. And of course I am indebted to Piccolo Nolan, the ultimate protector of Rocks and Nolans.

Support for this work was provided by AFOSR Grant FA9550-05-1-0050, with Dr. T. J. Beutner, Dr. R. Jeffries, and Dr. J. D. Schmisseur as program managers. Additional support was also provided by the Co-Op program at Wright-Patterson Air Force Base, as well as the MIT Lemelson Fellowship for minority engineers. Computational resources were provided by the Major Shared Resource Center at Wright-Patterson Air Force Base.

Effects of Upstream Wake Phasing on the Performance of Transonic Compressors

by

Sean P. R. Nolan

Submitted to the Department of Aeronautics and Astronautics on March 11, 2009, in partial fulfillment of the requirements for the degree of Doctor of Philosophy in Aeronautics and Astronautics

Abstract

The effect of the upstream wake phase on the work input (i.e., rise in stagnation enthalpy across the blade row) of a transonic rotor is examined computationally and analytically. It is found that the compressor work depends on the path followed by the wake vortices as they travel through the rotor passage. There can be an important impact on time-mean performance when the time-dependent circulation of the shed vortices in the wake is phase-locked to the rotor position. For the configurations tested, the calculated change in time-mean work input was approximately three percent.

The effect on work input is explained in terms of the influence of the time-mean relative stagnation pressure nonuniformity associated with the unsteady (but phase-locked) wake vortex flow field. Changes in vortex path mean that the position of this nonuniformity is altered relative to the rotor. There is lower pressure rise, and thus lower work, when the rotor blade is embedded in the region of low time-mean relative stagnation pressure than when it is immersed in a region of high relative stagnation pressure. In addition to this essentially two-dimensional effect, it is demonstrated that the locations of the wake vortex paths can have substantial effect on the tip clearance flow, implying potential impact on pressure rise capability and rotor stability limits. Model calculations are given to show the magnitude and nature of this phenomenon.

Thesis Supervisor: Choon S. Tan
Title: Senior Research Engineer, Gas Turbine Laboratory

Thesis Supervisor: John J. Adamczyk
Title: Senior Technical Specialist, NASA (ret.)

Thesis Supervisor: Edward M. Greitzer
Title: H. N. Slater Professor of Aeronautics and Astronautics

Thesis Supervisor: Mark Drela
Title: Terry J. Kohler Professor of Fluid Dynamics

Table of Contents

List of Figures

List of Tables

Nomenclature

Letters and Symbols

A	Area
B_3	A non-dimensional wake phasing parameter
C_p	Static pressure rise coefficient
F_θ	Tangential blade force per unit inlet flow area
H	Boundary layer shape factor
h	Enthalpy
L	Inter-bladerow spacing
M	Mach number
p	Pressure
q	Dynamic pressure
r	Radius
s	(1) Entropy
	(2) Streamwise coordinate
T	Temperature
t	Time
$\mathbf{u}$	Velocity
(u_x, u_y)	Velocity components in cartesian coordinates
W	Rotor pitch
w	Relative velocity magnitude
β	Angle between flow direction and axial direction
Δ	Change in quantity
δ^*	Boundary layer displacement thickness
ϕ	Flow coefficient
θ	(1) Angle between rotor shock and axial direction
	(2) Boundary layer momentum thickness

Ω	Angular velocity
$\boldsymbol{\omega}$	Vorticity
η	Adiabatic efficiency
ρ	Density
π	Total pressure ratio

Subscripts

E	Boundary layer edge
$defect$	Region of velocity defect
$exit$	Domain exit
$free-stream$	Freestream
$inlet$	Domain inlet
s	Static quantity
t	Stagnation quantity
1, 2	(1) Station numbers
	(2) Numbers denoting different states

Superscripts

AA	Area-average
MA	Mass-average
overbar (e.g. $\overline{u}$)	Mean
prime (e.g. u')	Perturbation quantity

Chapter 1

Introduction

1.1 Background

An important goal of research on aircraft engines is to reduce the size, weight, and complexity of the compressor core, without compromising compressor efficiency or stable flow range. One way to accomplish this goal is to reduce the number of blade rows and/or the number of blades within each blade row, while maintaining the same amount of work input for the compressor section. As indicated by the Euler Turbine equation below, to maintain the same work input for a given massflow with a reduced blade count, the remaining blades must be more highly-loaded and/or the wheelspeed must be increased.

$$Power = \dot{m}\Delta h_t = \dot{m}\Omega\Delta\left(ru_\theta\right). \tag{1.1}$$

The message from Equation 1.1 is that compressor design is being pushed into the realm of high loading and high Mach number. The flowfield associated with highly-loaded, high Mach number (HLHM) compressors is still not well understood, and the design of efficient HLHM compressors has proven to be difficult [1]. Furthermore, when an efficient design is achieved, the performance is often sensitive to small changes in geometry (increase in tip clearance, for example) or operating conditions (i.e. off-design performance) [2].

The research presented in this thesis gives insight into several aspects of the blade row interactions in HLHM compressors which cause the associated flowfields to be qualitatively different from those of low speed machines with light to moderate loading.

1.2 Previous Research

Enhanced unsteadiness and the presence of shock waves are two important aspects of blade row interactions in HLHM compressors that are not present low speed, moderately loaded compressors. These effects are seen as (at least) part of the reason why current compressor design methodologies have not translated well to HLHM compressors. For example, Ottavy [3, 4] demonstrated that for a transonic rotor geometry, the influence of the shock on the IGV wake is more significant than the influence of the rotor potential pressure field on the IGV wake. As a result, the effect of the rotor pressure field on the vane can be qualitatively different in a high speed machine compared to a low speed compressor. One of the results of this qualitatively different behavior is that compared to a low speed compressor flowfield, the HLHM compressor flowfield has a stator wake with greater unsteadiness and higher momentum defect.

Gorrell, et. al. developed the Air Force Research Laboratory's Stage Matching Investigation (SMI) Rig to examine mechanisms of blade row interaction in transonic compressors [5, 6]. This rig consists of a row of straight, thick inlet guide vanes (IGV) followed by a transonic stage. Key parameters of the rig are given in Table 1.1. The thickness of the IGV at the trailing edge is 11% of the rotor pitch at the midspan. The high loading and high relative Mach number of the rotor, compared to a low speed compressor, enhance the coupling between the rotor and the upstream vane row.

The magnitude of the blade interaction was found to be dependent on the inter-bladerow spacing. Computational and physical experiments with the SMI using different spacings between the IGV and the rotor were performed by Gorrell et al. Three different values of vane-rotor axial spacing were used: 0.29, 0.58, and 1.24 times the rotor pitch at the midspan, referred to as A, B, and C, respectively. The positions of the inlet guide vane are depicted in Figure 1.1, which shows the meridional view of the compressor geometry. For a fixed mass flow, the work input and efficiency were 1.6% and 0.6 points

Table 1.1: SMI Compressor Parameters

Parameter		Rotor Value
Inlet M_{rel} Tip		1.21
Aspect Ratio		0.961
Vane-Rotor Gap at Meanline (Fraction of Rotor Pitch)		
	A	0.29
	B	0.58
	C	1.24
Inlet Hub-to-Tip Ratio		0.750
Leading Edge Tip Diameter[m]		0.4826
Number of Rotors		33
IGV-to-Rotor Ratio		8/11
Design Stagnation Pressure Ratio		1.880
D Factor Hub		0.545

higher, respectively, for spacing C compared with spacing A.

Gorrell found that the reason for the performance change was that the wake vortices shed by the IGV were larger, had larger circulation, and had higher entropy difference (between the vortex core and the freestream) when the inter-bladerow spacing was reduced and the IGV was exposed to a stronger section of the shock. A model was proposed to describe the vortex shedding, based on the rotor bow shock passing by the trailing edge of the vane. The interaction between the shock and the IGV causes a change in net circulation (alternatively, a net loading) on the vane and hence, vorticity is shed by the vane. Another vortex (of opposite sign) is shed once the rotor shock has moved upstream of the vane, so the vane circulation returns to zero. Figure 1.2 is a schematic depicting the mechanism for the change in inlet guide vane loading. The difference in axial location at which the rotor shock intersects the upper and lower surface of the vane results, denoted as Δx, leads to an imbalance in pressures (and hence velocities) on the upper and lower surface. Therefore, when exposed to a stronger portion of the shock, the shed vortices are stronger, and the performance (specifically, efficiency and

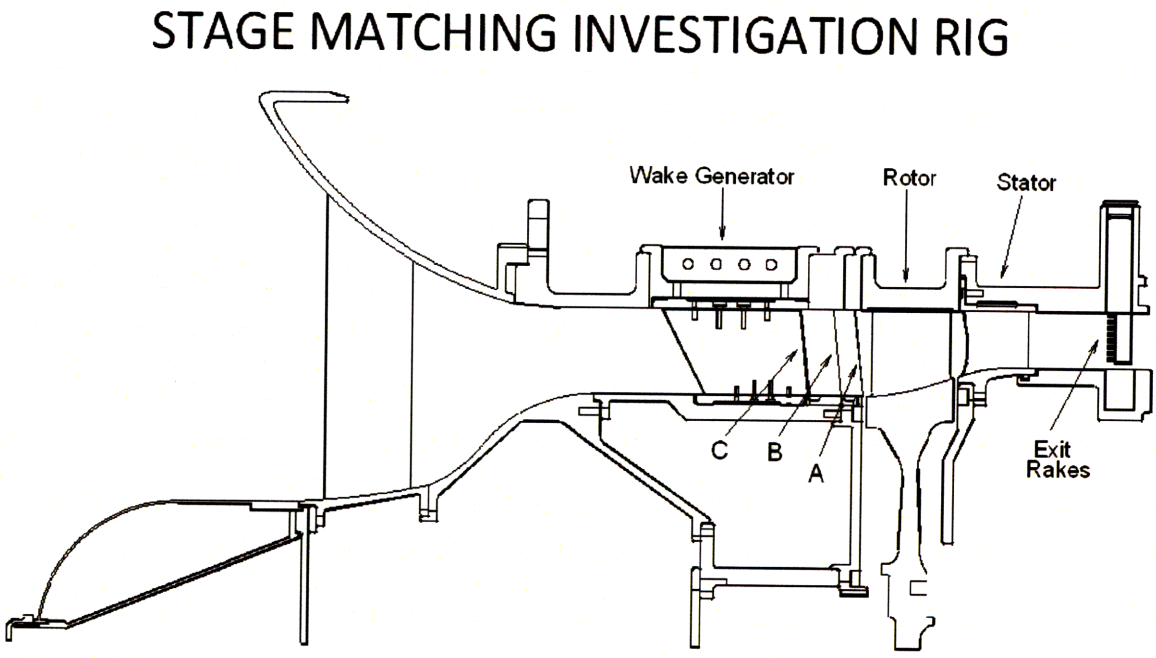

Figure 1.1: Stage Matching Investigation (SMI) Geometry. The SMI geometry consists of a vane row, a rotor row, and a downstream stator row. The gap between the vane and the rotor can be set at one of three values.

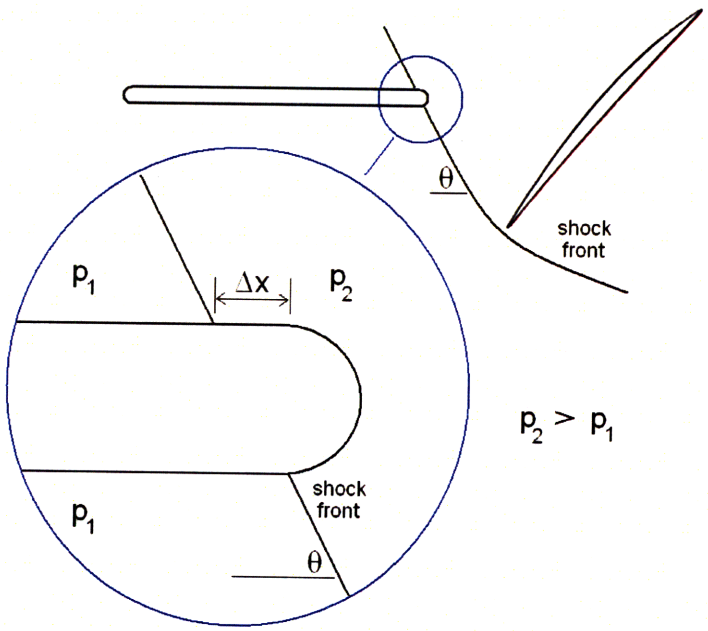

Figure 1.2: Illustration of vorticity generation mechanism associated with the interaction between the rotor shock and the upstream vane.

work input) is altered.

Figure 1.3 shows the vorticity contours at midspan for the SMI calculations done by Gorrell corresponding to spacing A and spacing C configurations; the intensity of the vortices in the spacing A configuration is greater than that in spacing C. In Figure 1.3 and throughout the thesis, the vorticity contours have been normalized by the freestream axial velocity divided by the rotor pitch, which is an approximate measure of the rotor blade circulation per unit area.

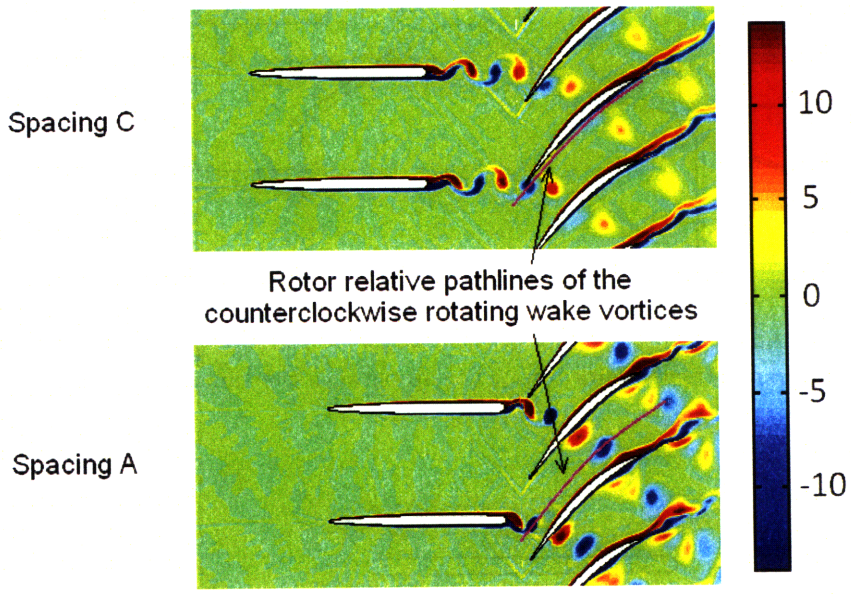

Figure 1.3: Vorticity contours (at midspan) in three-dimensional SMI IGV-rotor configuration at two different inter-bladerow spacings. The pink line shows the path of the counterclockwise rotating vortices in the rotor frame.

The trend of performance as a function of inter-bladerow spacing observed by Gorrell is opposite to the trends observed in investigations of low speed compressors. Smith [7], Hetherington and Moritz [8], and Mikolajczak [9] all observed greater efficiency and work input when the inter-bladerow spacing was reduced. Figure 1.4, which gives results of Hetherington and Moritz, is especially useful to highlight the difference between the behaviors of low speed and high speed compressors. The pressure ratio and efficiency curves show that an increase in the axial spacing between blade rows worsens the performance, compared to the nominal spacing, at low speed, while the same change in

geometry improves the high speed compressor performance. The improvement in low speed performance with reduced axial spacing has been shown by Smith [10] to result from reversible work transfer to the wake as it travels through the downstream blade row. This effect has also been described by Adamczyk [11], Greitzer, Tan, and Graf [12], and Valkov and Tan [13].

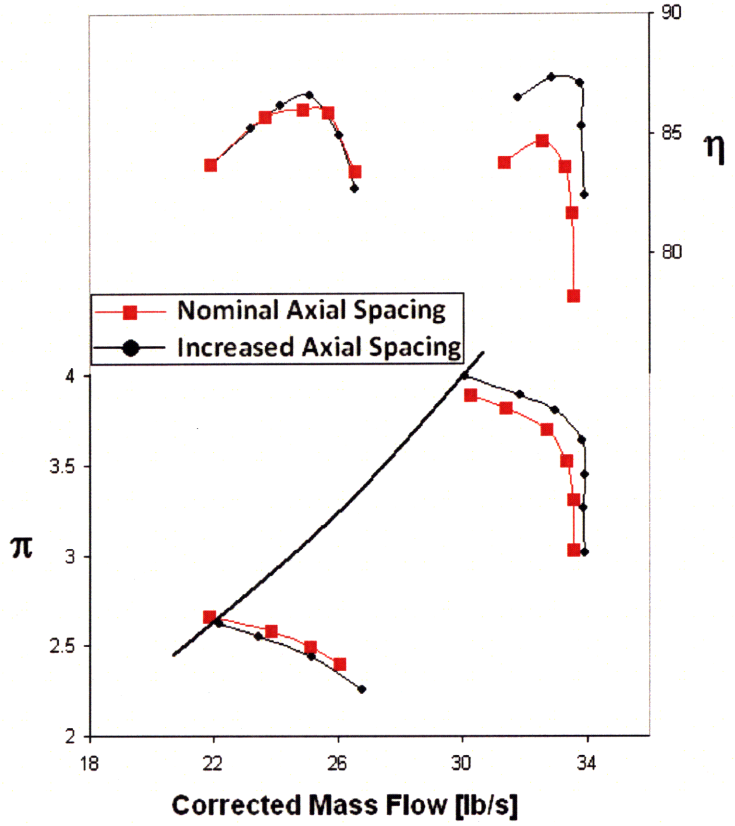

Figure 1.4: Results of Hetherington and Moritz: total pressure ratio (π)and adiabatic efficiency (η) versus mass flow are shown for two inter-bladerow spacing configurations at two different wheelspeeds. The relative performance of the configurations changes with wheelspeed.

Examination of Figure 1.3 reveals that not only is the strength (circulation, entropy) of the vane wake vortices altered by the change in spacing, but the relative path of the wake vortices through the rotor passage also changes. Because the rotor pressure field (specifically, the rotor bow shock) triggers the shedding of wake vortices, there is a specific relative path of the vortices through the rotor blade row for a given geometry and relative Mach number. The location of the path of the wake vortices through the

rotor passage will be referred to as the wake phase. The solid pink line in Figure 1.3 denotes the rotor relative path by which the counterclockwise rotating vortices travel through the rotor passage. In the configuration with spacing C, the path is adjacent to the pressure surface of the rotor blade. In contrast, when the inter-bladerow spacing is at spacing A the path of the counterclockwise rotating vortices passes through the midpitch of the rotor. The difference in wake phase will be shown in this thesis to contribute to the difference in performance trends of HLHM compressors.

Detailed analysis of the SMI flowfield by Botros [14] indicates that SMI performance changes due to alterations in the axial gap between IGV and rotor are closely linked to changes in the wake vortices. The examination of the dissipation within the shear flows and the shocks and the flux of entropy as a function of axial position that led to this conclusion is described in [14]. The work of Botros fortifies the observations made by Gorrell, et. al., but it goes further by using more quantitative measures to identify which aspects of the wake vortices are directly responsible for the change in performance that accompanies a change in inter-bladerow spacing. In addition to the change in the wake vortex strength [5] as one reason behind the change in performance, another reason is the change in the path by which wake vortices travel through the rotor [14].

Research of Zachcial and Nuernberger [15] includes numerical calculations that show the efficiency of a downstream rotor can be affected by the specific path of the phase-locked wake vortices shed from the upstream IGV. They performed numerical experiments on a two-dimensional geometry consisting of a stator followed by a rotor. The axial spacing between the blade rows was altered to change the rotor relative path of the stator wake vortices. At wheelspeeds such that the rotor relative Mach number is subsonic, maximum efficiency was achieved when the shed vorticity in the stator was positioned so that the induced velocity of the wake vortices reduced the edge velocity of the rotor boundary layer. The authors attributed the increased efficiency to reduced time-averaged skin friction. A similar trend in efficiency as a function of rotor relative

path of the stator wake vortices was observed when the wheelspeed was supersonic. In the supersonic case, however, the authors attributed the increase in efficiency to a reduction in the Mach number upstream of the shock, which reduced shock losses and the tendency of the suction side boundary layer to separate where the shock intersects the blade surface. While the work of Zachcial and Nuernberger is informative, it does not establish the causal link between vortex position and performance, nor does it describe the basic fluid dynamic scaling of the performance changes.

1.3 Research Questions

The purpose of this thesis is to determine the blade row interactions in HLHM compressors and to quantify the associated flow features that affect the performance of HLHM compressors. Pertaining to the blade row interactions, the specific research questions to be answered are:

- What is the impact of blade row interaction on efficiency and pressure rise capability for high-stage loading, high Mach number stages?
- What physical mechanisms govern the sensitivity of high loading, high Mach number stages to geometric and operational changes?
- What is the basic fluid dynamic scaling that characterizes the effects of coupling between blade rows in HLHM compressors?

1.4 Research Objectives

The specific aspect of the blade row interactions that the current research focuses on is the change in work input and peak pressure rise due to changes in wake phase. The objectives are defined to answer the research questions as they relate to the phenomenon of wake phasing. Thus, completing the research objectives will allow one to quantify the resulting change in work input due to wake phase change, explain the fluid mechanism

responsible for the change, and provide guidelines for determining the wake phase that results in a beneficial effect. Further, the effect of wake phase on the tip clearance flow and the subsequent changes in peak pressure rise will also be addressed.

The technical objectives addressed in this thesis are as follows:

- Assess the dependence of rotor work input on the path of the upstream wake vortices through the rotor, including formulating a simplified model to explain this unsteady phenomenon.
- Establish the fluid dynamic scaling that characterizes the sensitivity of the rotor work input to the path of the wake vortices.
- Assess the impact of the path of the wake vortices on the rotor tip clearance flow and the potential implications on stable operating range and pressure rise capability.
- Define design guidelines that can be used to adjust the path of the wake vortices to benefit compressor performance.

1.5 Technical Approach and Thesis Organization

To achieve the technical objectives, the following approach was taken. First, flowfields from the calculations of the Stage Matching Investigation (SMI) geometry were investigated in order to define the flow features of interest. The work of Gorrell, et. al. has aready identified several key flow features associated with the vane wake vortices, namely that (1) the vortices are triggered by the rotor bow shock, and (2) the strength or the vortices (i.e. vortex circulation and entropy difference between the wake vortices and the freestream) is greater when the inter-bladerow spacing is reduced. A more detailed examination of these flow features was done, and the features to which the performance is likely to be most responsive were isolated. In doing so, a simplified model to perform relevant wake phasing experiments was developed.

Using the information from three-dimensional numerical results, the geometry and boundary conditions were altered so that the specific flow features associated with the wake phase were isolated. From these three-dimensional results it was shown that the impact of wake vortices within the midspan of the rotor passage can be well-captured using a two-dimensional calculation. Unsteady two-dimensional calculations were thus performed to determine the relationship between the vane wake phasing and the compressor performance, and the mechanisms responsible for the relationship. The description and results of these calculations are described in Chapter 2.

Mechanisms associated with the wake phasing are discussed in Chapter 3. The understanding gained from the two-dimensional unsteady calculations was used to develop a steady flow description that captures the important influences of the vortical structures and the wake phase. With this approach a steady flow numerical experiment could be carried out in place of an unsteady flow numerical experiment. Two-dimensional steady calculations were performed to demonstrate the usefulness of the description. The steady flow description could be further simplified by treating the compressor as a simple diffuser, as is demonstrated through comparison to diffuser experiments.

The results and understanding established in Chapters 2 and 3 are used in Chapter 4 to develop guidelines for achieving a wake phase that mitigates the negative effects of the blade row interactions. In Chapter 5, a parametric study to determine the scaling of the effect of wake phasing with key flow parameters is given.

In Chapter 6, three-dimensional calculations (using the framework developed with the two-dimensional calculations) are performed to determine effects due to wake phasing on the tip clearance flow and the blockage at the rotor exit.

Chapter 7 summarizes the conclusions derived from this research work, and Chapter 8 suggests topics for future research related to wake phasing.

Chapter 2

Quantification of Wake Phasing Effects

2.1 Wake Phasing in SMI Compressor Flowfield

The observations about the SMI compressor flowfield made by Gorrell, et. al. [6] and Botros [14] indicate that the wake vortices are a crucial aspect of the SMI performance changes due to altering the axial gap between the IGV and rotor. Botros described a new aspect of why the wake vortices were important, namely, that changes in the path by which wake vortices travel through the rotor [14] can change the performance of a compressor. This chapter will show that a change in this vortex path can also be referred to as a change in the wake phase, and that this wake phase is important in setting the rotor work input.

Three-dimensional calculations show that the vortices within the vane wakes are evident over a large spanwise section of the three-dimensional rotor flowfield. Figure 2.1 shows a time-instantaneous plot of the vorticity at the 14% span to illustrate that even relatively close to the hub, phase-locked vortices are present in the flowfield. While there are some effects of changes in streamtube radial location and streamtube convergence, the three-dimensional calculations show that flow within the midspan section is essentially two-dimensional. For example, in the axial gap between the IGV and the rotor at the 14% span the angle between the velocity vectors and the $x - \theta$ plane is less than 15 degrees, even within the vortices. A first finding, therefore, is that the wake phasing phenomenon can be studied with the use of a two-dimensional numerical experiment.

Furthermore, in the three-dimensional SMI calculations done with spacing A, the increased dissipation function [14] relative to that of the spacing C configuration was greatest within the midspan, where two-dimensional modeling is especially applicable.

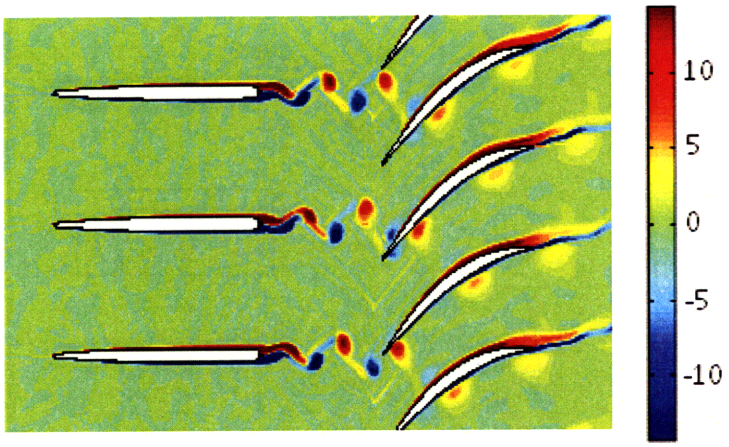

Figure 2.1: Vorticity contours at the 14% span of the SMI geometry with spacing C.

Dissipation within the rotor causes the mass-averaged entropy at the rotor exit to be greater than that at the rotor inlet, and this increase in entropy through the rotor is 17% larger with spacing A than with spacing C. The *rise* in entropy through the rotor passage as a function of span location is shown in Figure 2.2, where entropy is quantified as $T_{inlet}\Delta s/\left(0.5w_{inlet}^2\right)$. T_{inlet} is the temperature at the domain inlet, w_{inlet} is the rotor relative velocity at the inlet (at the blade tip), and Δs is the entropy relative to the entropy at the inlet of the computational domain. The hub is at 0% span and the casing in at 100% span.

Figure 2.2 shows that the rise in entropy is greater for the spacing A configuration than for spacing C over most of the rotor span, and this difference is greatest near the midspan. This (again) implies that key changes in the SMI flowfield resulting from the change in axial spacing occur over a majority of the midspan, and thus an unsteady two-dimensional calculation can capture the effect of wake phase on the rotor performance.

2.2 B_3: A Non-Dimensional Wake Phasing Parameter

Before discussing the changes in rotor performance that result from a change in vane wake phase, a parameter that quantifies the wake phase will be introduced. A change

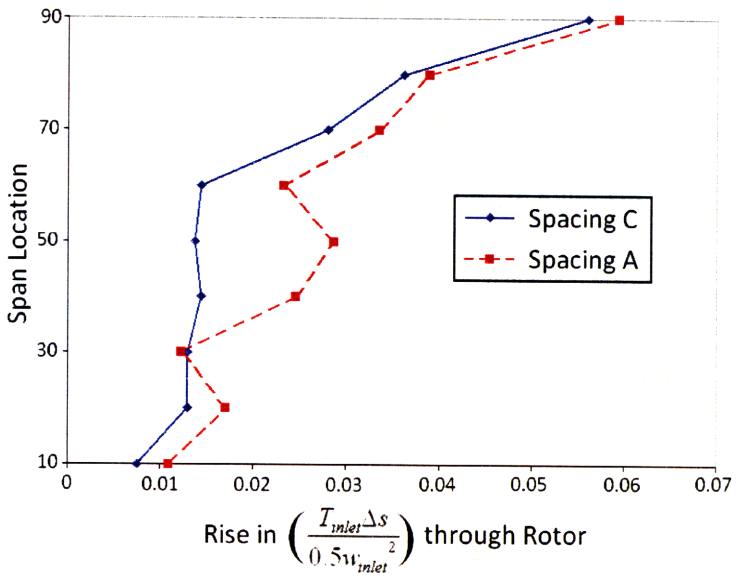

Figure 2.2: Profiles of the *rise* in pitch-averaged, mass-averaged value of $T_{inlet}\Delta s/\left(0.5w_{inlet}^2\right)$ from rotor inlet to rotor exit of the three-dimensional numerical experiments. Data sets for spacing C and spacing A are shown.

in this nondimensional metric, called the B_3 parameter (Botros [14]), implies a change in the vortex trajectory within the rotor passages.

Figure 2.3 illustrates the physical interpretation of the B_3 parameter. As indicated, time $t = 0$ occurs when the leading edge of the rotor blade is at the same pitchwise location as the vane being observed. From this reference point in time, the B_3 parameter is the ratio of the time when the *next* vortex pair shed by this vane enters the rotor passage to the time it takes for the rotor to move one pitch.

To estimate the time at which the next vortex pair shed by the inlet guide vane enters the rotor passage, one needs to account for the time until the next vortex pair begins to form, as well as the time needed to convect across the inter-bladerow spacing. Since the vortex formation is triggered by the impingement of the rotor shock on the inlet guide vane, the time at which the next vortex pair begins to form is the time at which the rotor shock impacts the trailing edge of the IGV. Relative to time $t = 0$, this event occurs at

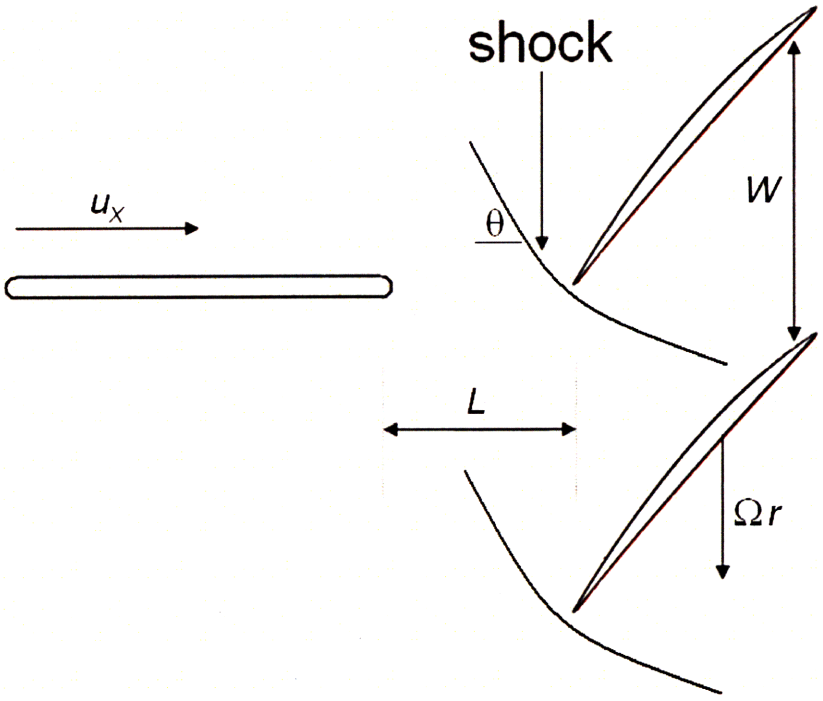

Figure 2.3: Relative position of vane and rotor at time $t = 0$.

$$t_{shock\_impact} = L\frac{\tan\theta}{\Omega r}, \tag{2.1}$$

where L is the length of the inter-bladerow gap, θ is the angle the rotor bow shock makes with the axial direction, and Ωr is the tangential velocity of the rotor at radius r. The time needed for this vortex pair to convect across the inter-bladerow gap is

$$\Delta t_{convect} = \frac{L}{u_x}. \tag{2.2}$$

where u_x is the axial convective velocity of the flowfield. Therefore, the time at which the vortex pair enters the rotor passage is

$$t_1 = t_{shock\_impact} + \Delta t_{convect} = L\frac{\tan\theta}{\Omega r} + \frac{L}{u_x}. \tag{2.3}$$

Finally, the time at which the rotor has moved one rotor pitch is

$$t_2 = \frac{W}{\Omega r} \tag{2.4}$$

where W is the length of the rotor pitch. As mentioned, the B_3 parameter is the ratio of t_1 to t_2, or, with ϕ denoting the flow coefficient $u_x/\Omega r$,

$$B_3 = \frac{L}{W}\left[(1/\phi) + \tan\theta\right]. \tag{2.5}$$

Each unit of B_3 corresponds to 2π radians (360 degrees) of the wake phase (or a pitchwise shift in the wake vortex path of one rotor pitch). Subsequently, values of B_3 that are whole numbers apart (such as 1.4 and 2.4) represent the same wake phase (i.e. the wake vortices follow the same trajectory through the rotor).

Equation 2.5 shows there are several ways to change the B_3 parameter of a compressor. In the unsteady calculations described in this chapter, B_3 is altered by changing the inter-bladerow spacing (L in Equation 2.5).

2.3 Numerical Experiment to Assess Effects of Wake Phasing

2.3.1 Computational Setup

A two-dimensional unsteady flow numerical experiment was used to demonstrate the effect of changes in wake phase on the rotor performance. The goal was to alter the phase of the IGV wake shedding without changing the strength (i.e., size and circulation) of the wake vortices, so that any subsequent changes in the compressor performance would only be the result of the change in wake phase. The first step was to calculate the unsteady flowfield associated with the 2D SMI geometry with spacing C. The inter-bladerow spacing, L, was then changed by a small amount (approximately 11%) to change the wake phase, B_3. A large change in wake phase (of approximately 180 degrees) was desired to achieve a large performance change due to change in wake phase. In general, a reduction in inter-bladerow spacing will also result in an increase in the strength

Table 2.1: 2D SMI Compressor Parameters

Parameter		Rotor Value
Inlet M_{rel} Tip		1.21
Vane-Rotor Gap (Fraction of Rotor Pitch)		
	Far	1.22
	Mid	1.09
IGV-to-Rotor Ratio		2/3
Design Stagnation Pressure Ratio		1.75
D Factor		0.535

of the wake vortices, since a stronger section of the rotor bow shock impinges on the IGV. However, it will be shown that the change in inter-bladerow spacing necessary to significantly change the phasing is sufficiently small so that the change in vane wake strength is negligible. The change in rotor performance, though, is large, showing that rotor performance is dependent on the wake phase. This result is crucial in explaining why the performance of HLHM compressors is sensitive to small changes in the axial spacing.

The 65% span section of the SMI rotor was chosen as a representative span for the SMI geometry. The geometry at a constant span of the SMI rotor is generally not at a constant radius, since the hub diameter varies with axial location and there is some distortion of the geometry in the transformation of this constant span into a two-dimensional grid. The distortion leads to a two-dimensional rotor geometry with higher camber compared to the original three-dimensional geometry, and therefore larger regions of separation. The distortion is less pronounced at higher spans, since the casing diameter of the SMI geometry is constant. By using the geometry at a location outboard of midspan (65%), the geometric distortion is reduced and a two-dimensional geometry representative of the SMI geometry is obtained. The parameters of this two-dimensional geometry are shown in Table 2.1.

The numerical experiment consisted of two IGV-Rotor configurations, with the dif-

Table 2.2: Number of Grid Points in 2D SMI Grids

Blade row	Axial	Radial	Pitchwise
IGV Far Spacing	230	2	61
IGV Mid Spacing	230	2	61
IGV Close Spacing	230	2	61
Rotor	189	2	81

ference between the two being a change in inter-bladerow spacing. One case has inter-bladerow spacing equal to that of spacing configuration C at the 65% span. The inter-bladerow gap equates to 122% of the rotor pitch at this span location, and will be referred to as "Far". The second case, which was designed to have a large difference in wake phase compared to the Far configuration, has an inter-bladerow spacing reduced (by 11%) to 109% of the rotor pitch; this configuration will be called "Mid". The number of gridpoints contained in the grids used for these two-dimensional calculations (including the "Close" configuration to be discussed later in Section 4.1) are indicated in Table 2.2.

The reduction in the B_3 parameter from the Far to Mid configuration is 0.42, corresponding to a change in phasing of 2.64 radians, or 151 degrees. The change in wake phase means the vortex path will be shifted nearly a half pitch in the tangential direction. Thus, the wake phase was changed significantly, while the strength of the wake vortices was changed very little, a result that will be confirmed in Section 2.3.3.

The change in wake path is depicted in Figure 2.4, which shows vorticity contours for both the Far and Mid configurations. The solid pink line denotes the rotor relative path of the counterclockwise rotating vortices. The pathline is closer to the rotor pressure surface for the Far configuration than for the Mid configuration.

General information pertaining to the execution of the experiment will now be described, followed by the results of the wake phasing experiment.

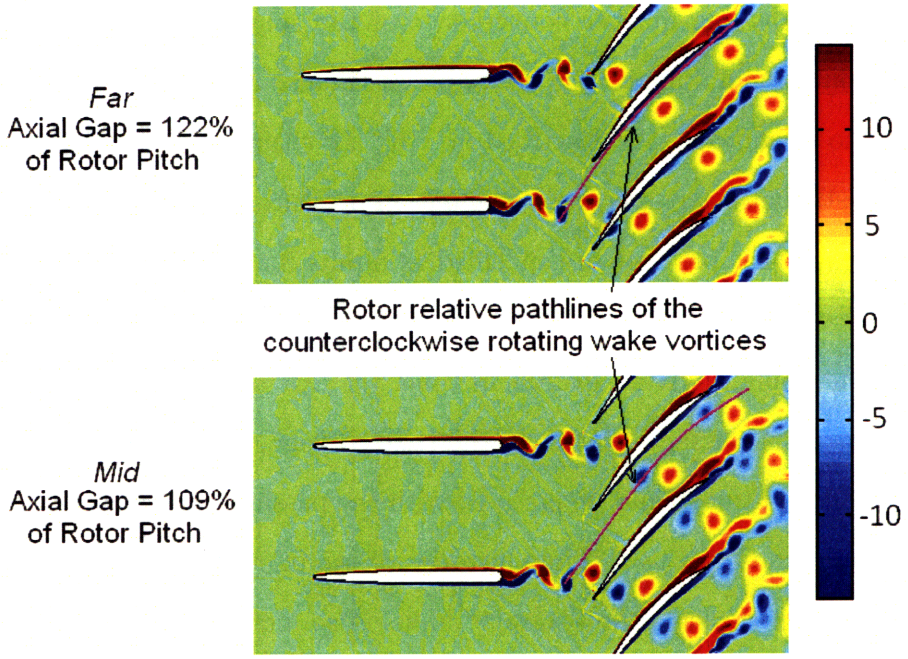

Figure 2.4: Vorticity contours in two-dimensional SMI IGV-rotor configuration at two different inter-bladerow spacings. The pink line shows the path of the counter-rotating vortices in the rotor frame.

2.3.2 Description of MSU Turbo Code

MSU Turbo [16] was used as the solver for these numerical experiments (and the three-dimensional calculations), with phase-lag boundary conditions applied on the tangential boundaries of the blade passages [17]. This type of boundary condition requires a computational domain of only one passage per blade row, regardless of the relative blade count of the blade rows. Therefore, when the blade counts of the blade rows are not equal to each other, the computational domain is reduced compared to a case where periodic boundaries are used. To perform a calculation on this two-dimensional vane-rotor compressor geometry using periodic boundary conditions, two vane passages and three rotor passages would have to be included in the computational domain because this is the smallest segment of the compressor annulus that includes a periodic sector of both the vane row and the rotor row. Using the phase-lag boundary condition, the calculation requires a computional domain of one vane passage and one rotor passage.

In addition to providing quicker convergence of the solution in this case, due to the reduced computational domain, the use of phase-lag also reduces the memory necessary to perform the calculation. As described in [16], a k-ϵ turbulence model was used. The domain inlet stagnation temperature, stagnation pressure, and absolute flow angle, and the domain exit static pressure are specified as inputs for the calculation.

Convergence was determined from the time history of the mass flow at both the inlet and exit of the domain. At an instant in time, the exit mass flow is dependent on the position of the rotor passage relative to the vane passage. Therefore, the exit mass flow for a converged solution should be periodic with the passing frequency of the inlet guide vanes relative to the rotor row. Time histories of the inlet and exit massflow were thus examined to ensure the signatures were periodic. Also, both the IGV inlet and the rotor exit should have the same time-averaged physical mass flow. When the inlet physical mass flow and the exit physical mass flow (time-averaged over one IGV passing) were within 0.1% of each other, the solution was deemed to be converged. Figure 2.5 shows the time history of the domain inlet and exit flow for a converged Turbo solution[1]. The curve representing the physical mass flow at the domain exit has a frequency equal to the IGV passing frequency.

The criterion used was that we needed to capture flow features that have a frequency twenty times greater than the rotor blade passing frequency, to ensure the blade wakes were accurately captured. According to the Nyquist sampling criterion, the sampling frequency must be twice as great as the feature that is being measured. This means that in order to meet the post-processing requirements, 40 samples of the flowfield must be taken for every rotor blade passing. Since the calculations were done with 160 timesteps corresponding to one rotor blade passing (and 240 timesteps corresponding to the vane passing frequency), the converged solution was sampled at every fourth timestep. Consequently, a time-averaged measurement from the flowfield consisted of

[1]The computational domain for the phase-lag calculation consists of one stator passage and one rotor passage, even though the smallest periodic sector contains two stators and three rotors. Thus, the fractional changes in mass flow at the domain exit are much larger than the mass flow fluctuations of +/- 1% at the exit of a periodic sector.

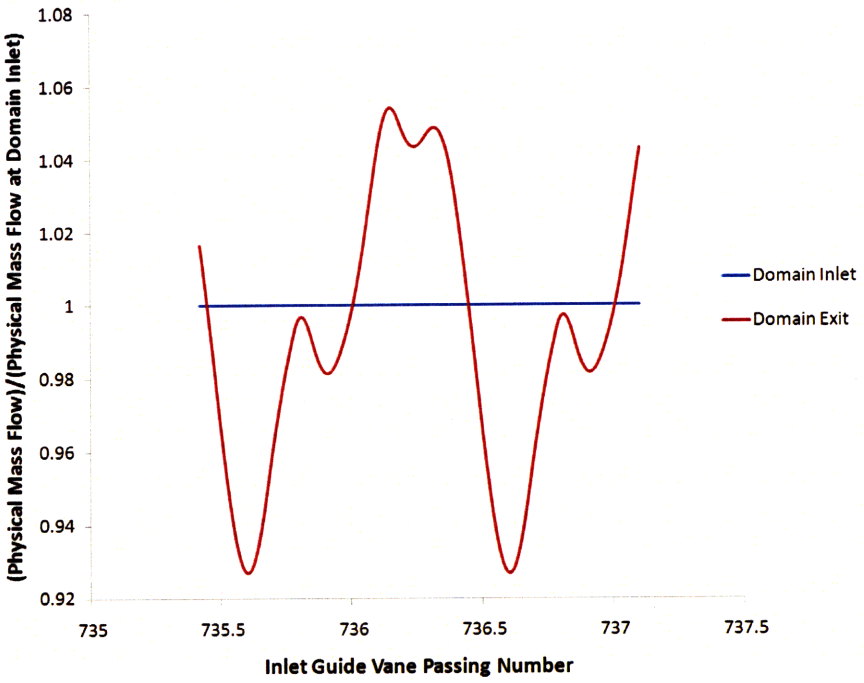

Figure 2.5: Mass flow histories, showing one per vane blade passing frequency periodicity of converged MSU Turbo phase-lag solution.

data averaged from 40 files in the rotor passage and 60 files in the IGV passage.

A collection of post-processing programs were used to measure from, and visualize, the flowfields calculated by Turbo. The raw data calculated from the cell centers was used in the post-processing of the results, rather than having Turbo output a plot3D formatted file. This avoided the loss in fidelity that occurs when the cell-centered solution is interpolated to the cell nodes in order to produce a plot3D solution file. Even though the cell center values were used, the nondimensionalization of the values was the same as plot3D variables, so the process by which the raw data is used to calculate the derived flow variables is well-documented. Fortran files were used to read in the Turbo output files and perform the calculations necessary to obtain the derived flow quantities. The derived flow quantities include such variables as stagnation pressure, stagnation temperature, Mach number, relative stagnation pressure, etc. The results of the post-processing calculations are then recorded by the Fortran program in a text file, which also includes any averaging (by area, time, or mass) that was specified in the post-

processing program. The text file is used as the input for a plotting script in Matlab. For more detailed information on the development and use of the post-processing codes, refer to Botros [14] and Villanueva [18].

2.3.3 Measure of Wake Strength

A perturbation velocity

$$u' = \sqrt{(u_x - \overline{u_x})^2 + (u_y - \overline{u_y})^2}, \tag{2.6}$$

was used as a nonuniformity metric to assess the wake vortex strength and flow nonuniformity. The overbar in Equation 2.6 represents a pitch- and time- average. When the quantity $(0.5\rho u'^2)$ is averaged over the pitch and in time, it represents (the incompressible estimate of) the stagnation pressure drop if the wake were to mix out at constant area, as described in the Appendix A of Botros' thesis [14]. Thus, after normalizing $(0.5\overline{\rho u'^2})$ by the inlet dynamic head, the metric of interest is:

$$\frac{\overline{0.5\rho u'^2}}{\overline{p_{t\_inlet}} - \overline{p_{inlet}}} = \frac{\frac{1}{\tau}\frac{1}{A_{total}}\int\left[\int 0.5\rho u'^2 dA\right]dt}{\overline{p_{t\_inlet}} - \overline{p_{inlet}}}. \tag{2.7}$$

At the rotor inlet, there is only 0.2 percent difference in this quantity between the Far and Mid configurations. However, there is a 23 percent difference in the nonuniformity metric at the rotor exit. Thus, even though the pitch-averaged, time-averaged, flow that enters the rotor passage is nearly identical in the two configurations, the rotor processes the flows very differently in the two cases because of the difference in wake phase. The conclusion we draw is that the difference in performance between the Far and Mid configurations results from the change in wake phase and not from changes in wake vortex strength.

2.3.4 Effects of Change in Wake Phase

The results of the unsteady calculations described in Section 2.3.1 are shown in Figure 2.6, which shows the adiabatic efficiency and the work input as a function of the corrected mass flow for three configurations: the isolated rotor, the IGV-rotor with Far spacing, and IGV-rotor with Mid spacing. In these plots, the mass-averaged (over time and passage area) values of stagnation temperature is used to calculate the rise in stagnation temperature across the rotor, and the mass-averaged stagnation pressure and stagnation temperature are used to calculate the adiabatic efficiency. The stagnation temperature rise is normalized by the inlet stagnation temperature, and the inlet corrected mass flow is normalized by the inlet corrected massflow for the isolated rotor at choke conditions.

To ensure an accurate calculation is made, the time-average is taken over one period of the inlet guide vane blade passing. At a corrected mass flow of 0.97, the work input of the rotor in the Far configuration is three percent greater than that of the Mid configuration. The efficiency for the Far configuration at a corrected mass flow of 0.97 was 0.1 points greater than that of the Mid configuration based on the state at the exit of the computational domain and 0.3 points greater based on a calculated mixed-out state. The small effect of the wake phase on efficiency is not the focus of this thesis, and the primary concern is to explain the dependency of rotor work input on wake phase. Appendix B briefly considers the relationship between wake phase and efficiency, and includes suggestions for future work on that topic.

2.4 Summary

Changes in the phase between the upstream wake vortices and the downstream rotor can have an effect on the rotor performance. The B_3 parameter [14] is introduced as a method for quantifying the wake phase. For the geometries examined, a reduction in

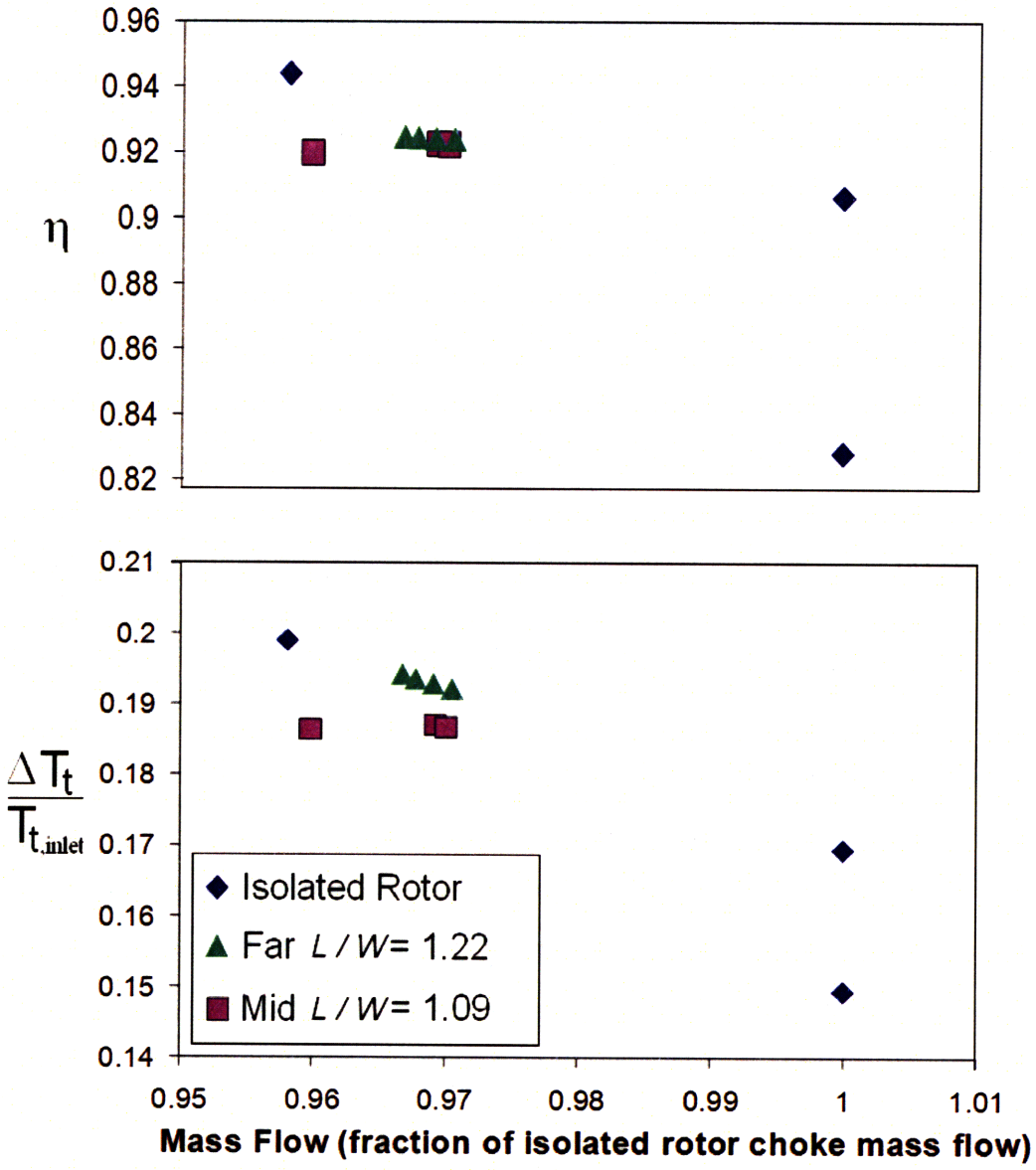

Figure 2.6: Efficiency and stagnation temperature rise vs. mass flow for the isolated rotor, and the Far and Mid geometries.

B_3 of 0.42 resulted in a 3% reduction in the rotor work input.

Chapter 3

Charactarizing Effects of Wake Phasing

3.1 Steady Flow Representation of Wake Vortices

To understand why the change in the wake trajectory within the rotor causes a change in performance, it is useful to consider the flowfield in the rotor reference frame. The unsteady wake appears as a train of counter-rotating vortices as shown in Figure 3.1a (see also Figure 2.4). It will be shown that the time-average footprint of the vortex street is a stratification of relative stagnation pressure upstream of the rotor. Two methods of showing this (from Crocco's theorem and from a kinematic argument) are described below.

3.1.1 Time-Mean Footprint of the Wake Vortices: I - Crocco's Theorem Description

Each IGV sheds counter-rotating vortices which move through the rotor as illustrated in Figure 3.1a. The blue lines in Figure 3.1 denote the rotor relative paths of the wake vortices. The vortex pairs along these lines have been shed from different IGVs and therefore have entered the rotor passage at different times. By applying Crocco's Theorem in the rotor reference frame, the time-mean impact of the wake vortices on the relative stagnation pressure variation can be discerned.

We define $\mathbf{u}'$ as the difference between the instantaneous velocity and the time-mean velocity and $\boldsymbol{\omega}'$ as the pertubation vorticity. The expression for the variations in time-mean stagnation enthalpy and in entropy is given by

$$\overline{\mathbf{u}' \times \boldsymbol{\omega}'} = \nabla \overline{h_t} - \overline{T \nabla s}, \tag{3.1}$$

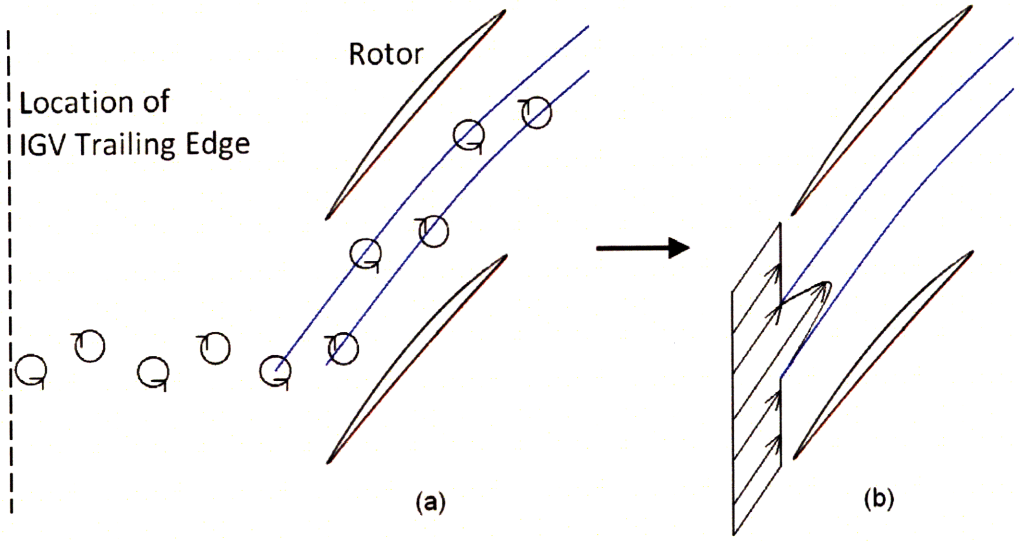

Figure 3.1: Unsteady vortex flow field (a) and time-mean (b) representations of rotor flowfield. The blues lines show the path of the vortices in the rotor frame. The fluid between the blue lines has the highest time-mean relative stagnation pressure.

where the overbar denotes a time-average.

Although there is an entropy gradient associated with the shed vortices, the calculations confirm that the $\overline{T \bigtriangledown s}$ term in Equation 3.1 is five to six times smaller than the other terms in the equation. Thus, the last term in Equation 3.1 is negligible and can be ignored. Furthermore, $\bigtriangledown h_t$ can be approximated as $\bigtriangledown p_t / \rho_t$. Thus the time-mean stagnation pressure variation in the regions of uniform entropy is given by

$$\overline{\mathbf{u}' \times \boldsymbol{\omega}'} = \overline{\left(\frac{\bigtriangledown p_t}{\rho_t} \right)} \approx \frac{\bigtriangledown \overline{p_t}}{\overline{\rho_t}}. \tag{3.2}$$

The implication of Equation 3.2 is that the unsteady rotor inlet flow containing the discrete vortices can be approximated as a steady pitchwise nonuniformity in the stagnation pressure. This result is shown in Figure 3.1b, where the fluid between the vortex pathlines has a higher time-mean relative stagnation pressure than the fluid outside of the pathlines.

A quantitative view of the time-mean variation given by contours of time-averaged relative stagnation pressure is seen in Figure 3.2, which has been extracted from unsteady

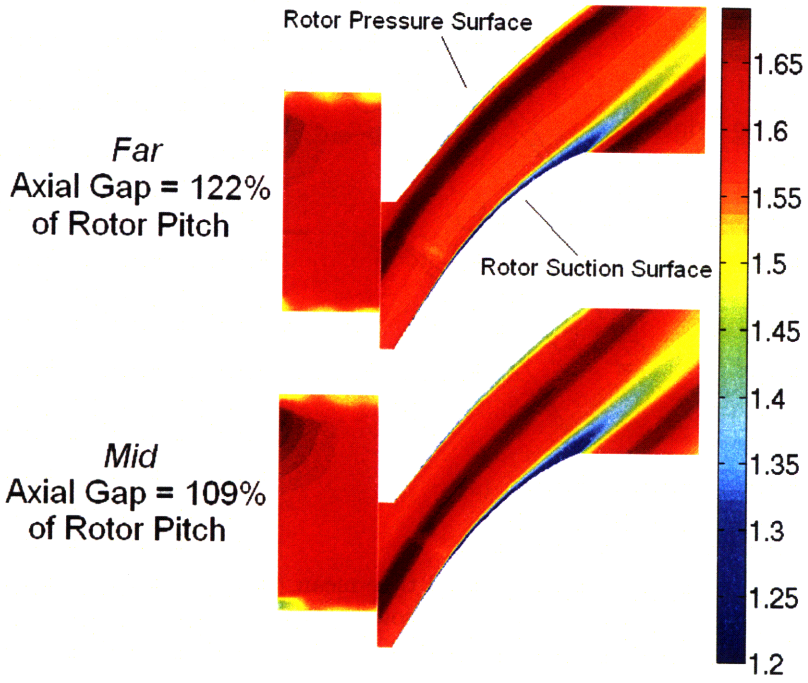

Figure 3.2: Time-mean relative stagnation pressure contours for Far and Mid geometries.

calculations for the Far and Mid configurations. The relative stagnation pressures shown in Figure 3.2, and throughout the thesis, have been normalized by the absolute stagnation pressure upstream of the IGV row. Although the *profile shape* of the time-mean relative stagnation pressures is similar in the Far and Mid configurations, the pitchwise *locations* of the profile relative to the rotor are very different because of the difference in wake phase.

3.1.2 Time-Mean Footprint of the Wake Vortices: II - Kinematic Arguments

A kinematic argument, applied in the rotor relative frame, can also be used to estimate the time-averaged relative stagnation pressure stratification of the wake vortices. The essentially (for these purposes) inviscid flow can be viewed as a mean flow with counter-rotating vortices convecting through the rotor passage. Superposing the relative velocity vectors from the mean flow and from the wake vortices, the relative velocity within

the rotor passage is found to be greatest between the pathlines of the counter-rotating vortices, as is depicted in Figure 3.1. Since the fluid particles on the circular streamlines or the vortices have an approximately constant static temperature, the fluid between the vortex pathlines thus has a greater stagnation temperature than the slower fluid [12]. The stagnation temperature difference between the freestream and the center of the vortex street can be approximated by

$$\frac{c_p(T_t - T_{t,0})}{0.5u_0^2} = \frac{2\Gamma}{u_0 W}\frac{u_v}{u_0}, \tag{3.3}$$

where $T_{t,0}$ and u_0 are the stagnation temperature and velocity of the fluid upstream of the IGV, Γ is the circulation per unit span of the vortex row, and u_v is the convective velocity of each vortex [12]. The isentropic flow relationship between stagnation temperature and stagnation pressure allows an estimate of the time-mean stagnation pressure profile. For the Far configuration calculation described in Section 2.3.1, the variation in time-mean relative stagnation pressure across the pitch of the rotor inlet is estimated to be 14% of the relative stagnation pressure at the domain inlet, compared to the computed value of 10%.

3.1.3 Time-mean Relative Stagnation Pressure Profile

The message of Sections 3.1.1 and 3.1.2 is that the change in vortex trajectory between the two configurations (Far and Mid) appears in the time-averaged flowfield as a change in the pitchwise location of the regions of high and low relative stagnation pressure. In other words, the time-mean of the unsteady flowfield in Figure 3.1a is the steady flowfield in Figure 3.1b. This interpretation captures the important aspects of the unsteady wake vortices and changes in wake phase; changes in wake phase change the position of time-mean relative stagnation pressure profile relative to the rotor, influencing the capability of the rotor blade boundary layers to negotiate the rotor pressure rise. Specifically, the lower the relative stagnation pressure fluid that encases the rotor the

larger the exit boundary layer displacement thickness and deviation. The result is a lower diffusion capability, and consequently a lower work input. If the circulation of the wake vortices becomes greater, the amplitude of the relative stagnation pressure, and therefore the potential influence of wake phasing on rotor performance, increases. The link between the relative stagnation pressure adjacent to the rotor blade and the rotor performance is discussed in Section 3.2.

3.2 Link Between Relative Stagnation Pressure Profile and Integral Boundary Layer Quantities

As shown above, a change in phasing changes the relative stagnation pressure adjacent to the blade surface. This in turn affects the integral quantities of the blade boundary layer. The link between the relative stagnation pressure of the fluid adjacent to the blade and the change in the blade boundary layer characteristics is the boundary layer edge velocity u_E. If high stagnation pressure fluid is adjacent to the blade, the boundary layer edge velocity will be high. Conversely, low stagnation pressure fluid results in a lower edge velocity.

The effect of edge velocity on boundary layer integral quantities can be qualitatively demonstrated using the Von Karman integral momentum equation given in Eqn. 3.4. Subsequent numerical experiments (to be presented in Chapter 5) will provide the precise quantitative measures to back up this qualitative analysis.

$$\frac{d\theta}{ds} - (H+2)\frac{\theta}{\rho u_E^2}\frac{dp}{ds} = \frac{C_f}{2}. \tag{3.4}$$

In Eqn. 3.4, s is the streamwise coordinate, θ is the momentum thickness of the rotor boundary layer, H is the boundary layer shape factor, u_E is the boundary layer edge velocity, and C_f is the skin friction coefficient. In the situations considered the change in pressure gradient is sufficiently small (less than 5%) that for the present purpose we assume that pressure gradient is unchanged for the different values of boundary layer

edge velocity. Further, if the adverse pressure gradient is large enough, the skin friction coefficient in Equation 3.4 will not be significant except very near the leading edge of the blade. For this discussion we assume this is the case and neglect skin friction. Applying these assumptions, taking a mean value for the shape factor, and rearranging the integral equation results in an expression for the fractional change in displacement thickness between two arbitrary stations 1 and 2.

$$\frac{\delta_2^*}{\delta_1^*} = exp\left\{(H_{mean}+2)\int_1^2 (dp/\rho u_E^2)\right\}. \tag{3.5}$$

For a given pressure rise, the fractional change in the boundary layer displacement thickness is larger when the boundary layer edge velocity is smaller; larger boundary layer displacement thicknesses lead to less diffusion capability. If the skin friction coefficient had not been neglected, the resulting Equation 3.5 would have been more complex, but the qualitative trend between u_E and δ_2^*/δ_1^* would have been the same. In summary, the wake phase affects the level of relative stagnation pressure that is seen by the rotor blade. The change in boundary layer characteristics observed create a change in pressure rise and work input of the rotor.

3.3 Steady Model and Related Flow Phenomena

3.3.1 Numerical Experiment of Steady Model

In this section we show that a steady calculation that emulates the (simplified view of the) unsteady calculations produces trends similar to those found in the unsteady computations. That is, trends in work input similar to those obtained by changing the phase of the wake vortices can be achieved by shifting the pitchwise position of a steady relative stagnation pressure nonuniformity. Specifically we show that the relationship between wake phase and performance in the unsteady flow can be well-captured with a steady flow description.

To show this, the time-averaged flow profile measured at an axial station near the

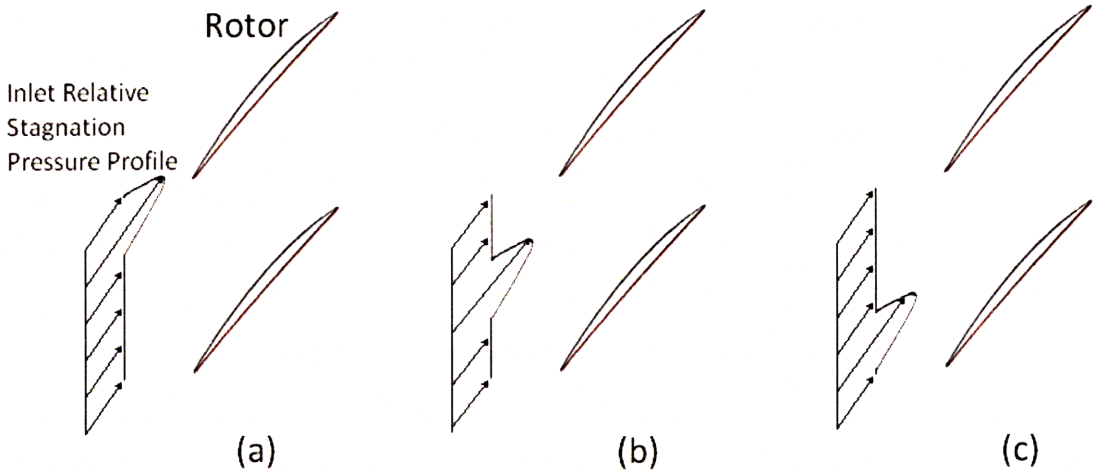

Figure 3.3: Three different inlet pitchwise positions (denoted (a), (b), and (c)) for the relative stagnation pressure profile.

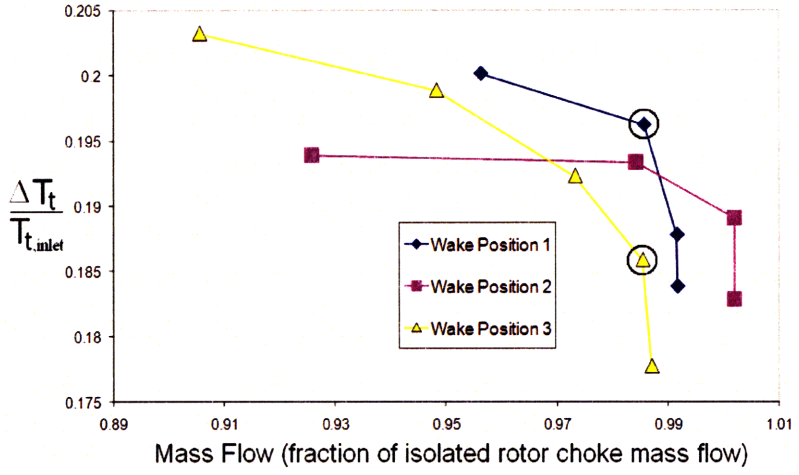

Figure 3.4: Stagnation temperature rise vs. mass flow from steady computations. The relative stagnation pressure contours corresponding to the circled data points are shown in Figure 3.5.

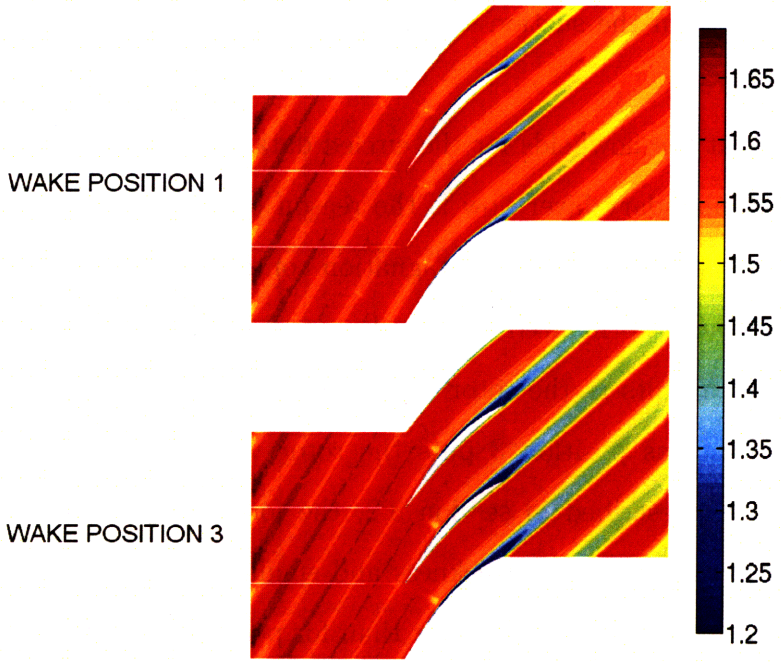

Figure 3.5: Relative stagnation pressure contours for steady calculations, wake position 1 (high stagnation pressure fluid over blade), and wake position 3 (low stagnation fluid over blade). These contours correspond to the circled data points from Figure 3.4.

rotor inlet (10% of the rotor chord upstream of the rotor leading edge) of the unsteady MSUTurbo computations was used as the inlet condition for a steady isolated rotor calculation. The profile was specified to move at the same tangential velocity as the blade, so the flow was steady in the frame of the rotor. Calculations were performed with the same profile located at three different pitchwise positions relative to the rotor, equally spaced across the pitch. Sketches of the three profile positions are given in Figures 3.3a, b, and c.

The results of this numerical experiment are indicated in Figure 3.4, which shows the absolute stagnation temperature rise, normalized by the inlet absolute stagnation temperature, across the rotor as a function of the inlet mass flow. The three data sets in Figure 3.4 refer to the three different position of the inlet flow profile. The difference in inlet profile position is seen to produce a change in rotor performance similar to that in the unsteady computations in Figure 2.6. For a given corrected mass flow, the work

input is greatest when the suction side is bathed by fluid having the highest relative stagnation pressure.

A closer look at the flowfields for the circled data points in Figure 3.4 also confirms that the altered boundary layer flow is the reason behind the change in performance. Figure 3.5, which shows the relative stagnation contours for wake position 1 and wake position 3, both at a normalized corrected mass flow of 0.984, depicts the situation. Profile position 1 results in the rotor blade being encased in high relative stagnation pressure fluid, whereas position 3 puts the rotor within the low relative stagnation pressure fluid. As described in section 3.2, the former has a suction side boundary layer with smaller displacement thickness and smaller deviation than the latter. The work input for position 1 is 5.3% greater than for position 3 at the nondimensionalized corrected mass flow of 0.984.

3.3.2 Connection with Experiments on Nonuniform Flow in Diffusers

The trend of increased work input when a region of high stagnation pressure fluid is adjacent to the rotor is consistent with the results from two-dimensional diffuser experiments by Wolf and Johnston [19, 20]. In these experiments, an inlet profile was positioned to produce either (1) high stagnation pressure fluid on the diffuser walls or (2) low stagnation pressure fluid on the walls. The profiles used in the experiment are shown in Figure 3.6, which gives the velocity as a function of pitch location. The abscissa values of 0 and 1 correspond to the walls of the diffuser.

When the fluid with the greatest velocity magnitude (and therefore greatest stagnation pressure) was placed adjacent to the diffuser walls, the diffuser produced a larger pressure rise than when the fluid with lowest velocity magnitude (and therefore lowest stagnation pressure) was placed adjacent to the diffuser walls; the increased boundary layer edge velocity resulted in smaller boundary layer displacement thicknesses and hence greater effective exit flow area. The pressure rise coefficient for both inlet profiles for

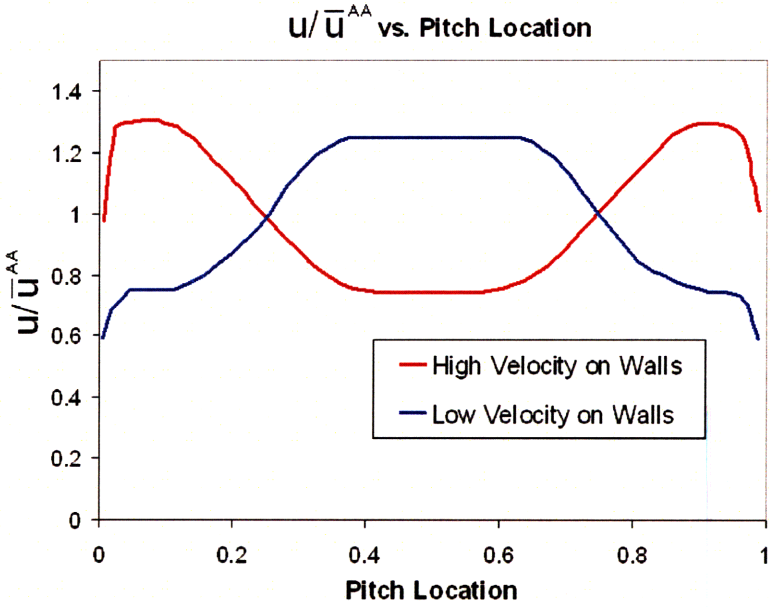

Figure 3.6: Inlet profiles used in Wolf and Johnston's experiments.

different diffuser area ratios are shown in Figure 3.7.

For the rotor passage, the ability to sustain a higher pressure rise coefficient corresponds to a greater work input. A control volume analysis, given in Appendix A, shows that the difference in pressure rises measured by Wolf and Johnston correspond to tangential force changes roughly comparable to those calculated in the computational experiments discussed here. In summary, the basic links between wake phase and work input can be qualitatively described in terms of a two-dimensional diffuser flow.

3.3.3 Clocking

If the unsteady wake vortices are interpreted as creating a time-averaged profile of relative stagnation pressure entering the rotor, the effect of changes in wake phase can be viewed as similar to the effect of changes in *clocking*. Clocking refers to the pitchwise relative positioning of two blade rows with the same wheelspeed and can apply to rows of stators or rows of rotors on the same spool. Depending on how two blade rows are clocked, the wake from an upstream row will take a different path through a downstream

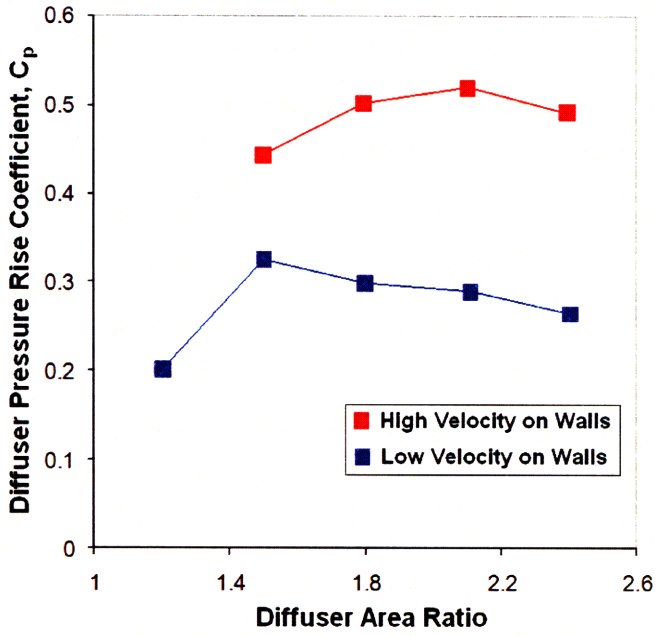

Figure 3.7: Diffuser pressure rise coefficient, C_p vs. diffuser area ratio for two different inlet velocity profiles. (Results of Wolf and Johnston, as reported by Greitzer, Tan, and Graf [12]).

row.

Figure 3.8 illustrates how clocking works using the example of two rotor rows. In Figure 3.8a, the two rotors depicted are clocked such that the wake (low relative stagnation pressure fluid, marked in this figure by blue lines) from the upstream blade row passes directly adjacent to the suction surface of the downstream blade row. Note that there is another blade row between the two blade rows shown, but the middle blade row, which is not moving, is represented by by an empty space in the figure. In Figure 3.8b, the clocking of the rotor blade rows has been altered such that the wake from the upstream rotor now passes through the midpitch of the downstream rotor. Such changes in clocking can alter the performance of a downstream rotor.

Key [21] found that for a highly-loaded compressor stage, the wake shed by the downstream stator was separated when the wake from the upstream blade row impinged upon the downstream stator, leading to reduced efficiency. Although the current research focuses on work input rather than efficiency, the results Key obtained from the highly-

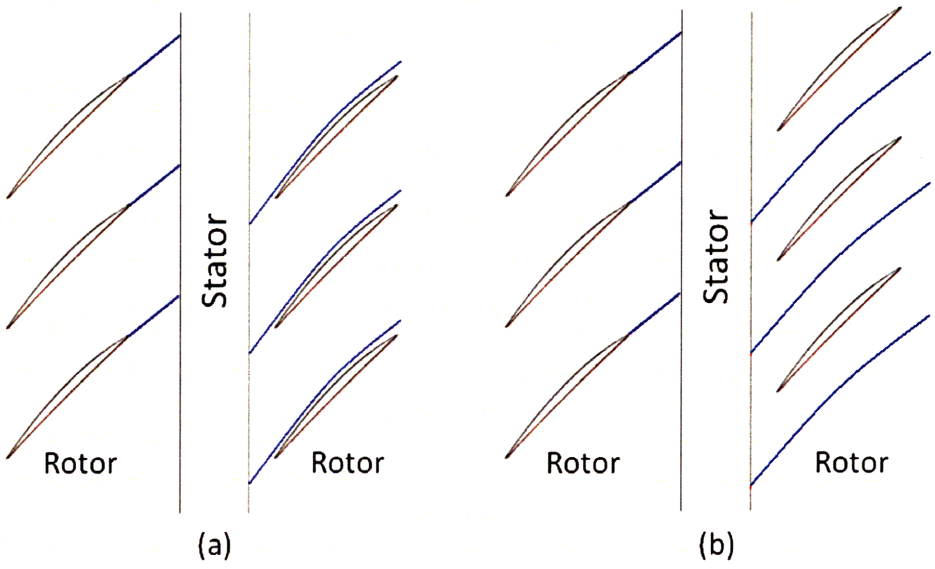

Figure 3.8: Two different clocking positions for rotor blades. The two rotors shown are moving at the same wheelspeed. In (a), the clocking between the two bladerows is different than in (b), because of a shift in the relative pitchwise positions of the blade. The colored lines represent the rotor relative paths of the wakes produced by the upstream rotor.

loaded stage are consistent with the concepts described in this thesis.

3.4 Independence of the Results to the Inlet Profile of Stagnation Temperature.

The Munk and Prim substitution principle [12] states that for a steady, inviscid flow, the streamline pattern and static pressure field is independent of the inlet stagnation temperature profile. The same principle also applies to viscous flows in which the stagnation pressure change due to viscous work is equal and opposite to the stagnation pressure change due to heat transfer [22]. However, the magnitude and nature of viscous effects in the compressor flow were not known well enough to determine a priori whether the substitution principle was applicable. Therefore, numerical calculations were used to determine whether the substitution principle was still applicable to the model calculations described in Section 3.3.1.

To test for the dependence on inlet relative stagnation temperature profile, two dif-

ferent stagnation temperature profiles were used for the same inlet relative stagnation pressure profile. In one case, the stagnation temperature profile at the inlet was uniform, i.e. the inlet flow was isenthalpic. In the other case, the stagnation temperature profile was such that the inlet profile was nearly isentropic. The compressor performance change due to shifts in inlet profile position was similar in both cases. Figure 3.9 shows the stagnation temperature rise vs. mass flow for two different inlet wake positions, with each profile position run with both the isenthalpic inlet profile and the isentropic inlet profile. At a mass flow of 0.98, the variation in work input between the two positions was nearly the same for both stagnation temperature profiles, with the maximum difference in the variation less than 12% of the variation itself.

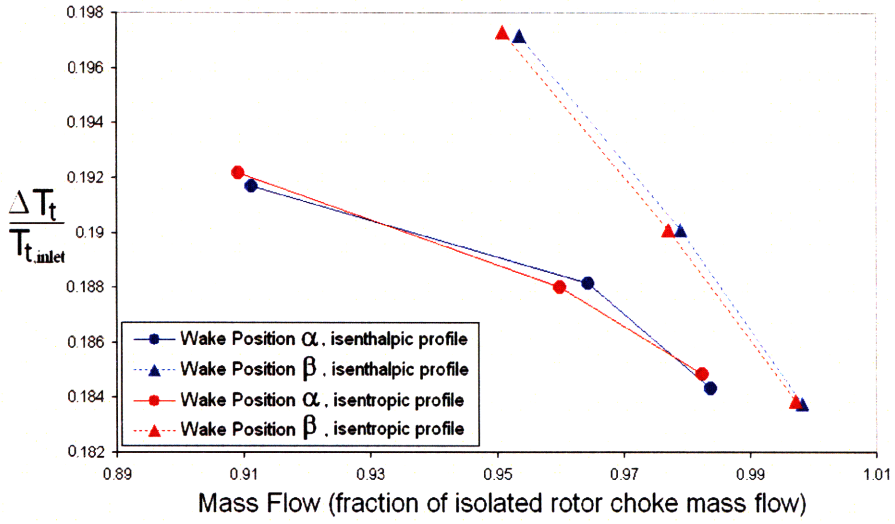

Figure 3.9: Stagnation temperature rise across the rotor for two different inlet wake positions. There are two data sets for each wake position. One data setcorresponds to an isenthalpic inlet profile and the other to an isentropic inlet profile.

The parametric studies to be described in Section 5.2 used an isenthalpic inlet flow profile. Nevertheless, the dependence of the performance on shifting of the relative stagnation pressure profile was comparable to the results from Section 3.3.1, which used a roughly isentropic inlet flow profile, thus providing further evidence that the effect of the stratification in relative stagnation pressure is approximately independent of the

stagnation temperature profile.

3.5 Summary

The presence of wake vortices in the time-accurate vane-rotor flowfield results in a stratification of relative stagnation pressure in the time-mean flowfield. A change in the wake phase changes the pitchwise position of the stratification. Thus, a change in wake phase in the unsteady vane-rotor geometry can be modeled by a shift in relative stagnation pressure profile at the inlet of an isolated rotor. The link between the wake phase and the rotor performance is the rotor boundary layer. High values of time-mean relative stagnation pressure fluid adjacent to the rotor surface means a higher boundary layer edge velocity, resulting in reduced boundary layer displacement thickness and deviation, and thus increased diffusion capability. It is also found that the effect of wake phasing is roughly independent of the stagnation temperature profile.

Chapter 4

Possible Beneficial Reduction in Vane-Rotor Gap

4.1 Guidelines for Control of Wake Phase

Previous blade row interaction research studies, referenced in section 1.2, showed that in a high-speed compressor, the blade row interactions are such that the work input and efficiency decrease with reduced vane-rotor gap. However, based on the ideas presented in Chapters 2 and 3, it should also be possible for a reduction in vane-rotor gap to result in an improvement in performance. For this to occur, however, the reduction in spacing must lead to a beneficial change of the wake phase that is large enough to outweigh any detrimental effect of the increase in wake strength due to reduced blade row spacing. To show the possibility for using wake phase to improve performance with reduced inter-bladerow spacings, and as a means of further validation, the logic derived from the analysis in Chapter 3 is used to improve the performance of the two-dimensional IGV-Rotor configuration (i.e. the phase is chosen so the region of greatest time-mean relative stagnation pressure is adjacent to the rotor suction surface). The B_3 parameter was used to calculate by how much the vane-rotor spacing from the Mid configuration should be reduced in order to set up a beneficial wake phase and improve the compressor performance.

The same basic geometry of an IGV row upstream of a rotor used in the previous two-dimensional unsteady Turbo calculations is used here. As mentioned above, the Mid configuration (axial spacing equal to 109% of the rotor pitch) was used as the baseline. The location of the peak time-averaged relative stagnation pressure for this case was near the midpitch, representing a wake phase that produces the worst performance, with the location of the peak relative stagnation pressure at 45% of the rotor pitch from

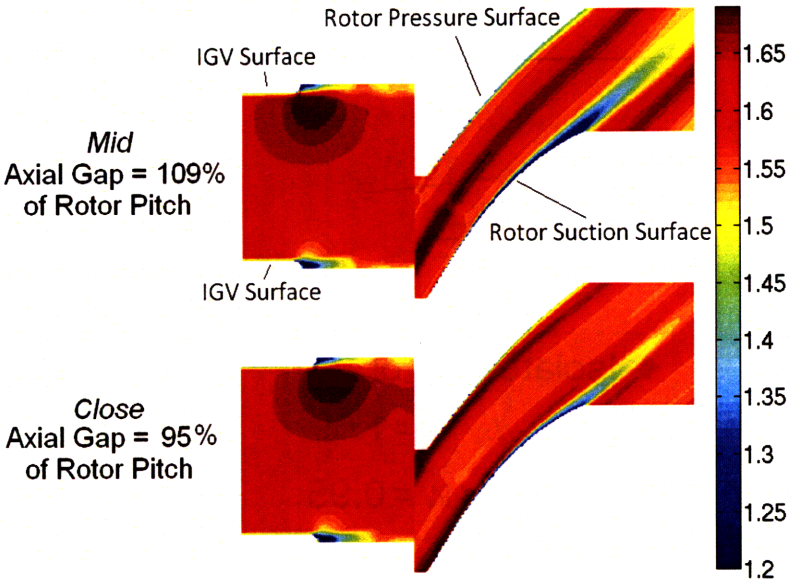

Figure 4.1: Time-mean rotor relative stagnation pressure contours for Mid and Close geometries.

the rotor suction surface. To move the peak relative stagnation pressure fluid to the suction surface a reduction in B_3 of 0.45, or a 162 degree change in phasing, was needed. Using Equation 4.1, which is just Equation 2.5 rearranged, this phase was found to be attained with an inter-bladerow spacing reduction of 13%, resulting in an inter-bladerow spacing equal to 95% of the rotor pitch. This spacing will be referred to as the "Close" configuration.

$$\Delta L = \frac{\Delta B_3 \cdot u_x W}{\Omega r + u_x \tan\theta}, \tag{4.1}$$

The time-mean relative stagnation pressure contours corresponding to the Mid and Close configurations are shown in Figure 4.1. Compared to the Mid configuration, the suction side boundary layer displacement thickness at the rotor exit in the Close configuration is 18% smaller, resulting in a 4% improvement in work input, as is seen in the plot of stagnation temperature rise vs. mass flow in Figure 4.2. As in Section 2.3.4, the increase in efficiency was much smaller, 0.1%. Linear interpolation was to used to define the difference in stagnation temperature rise and efficiency at a common mass

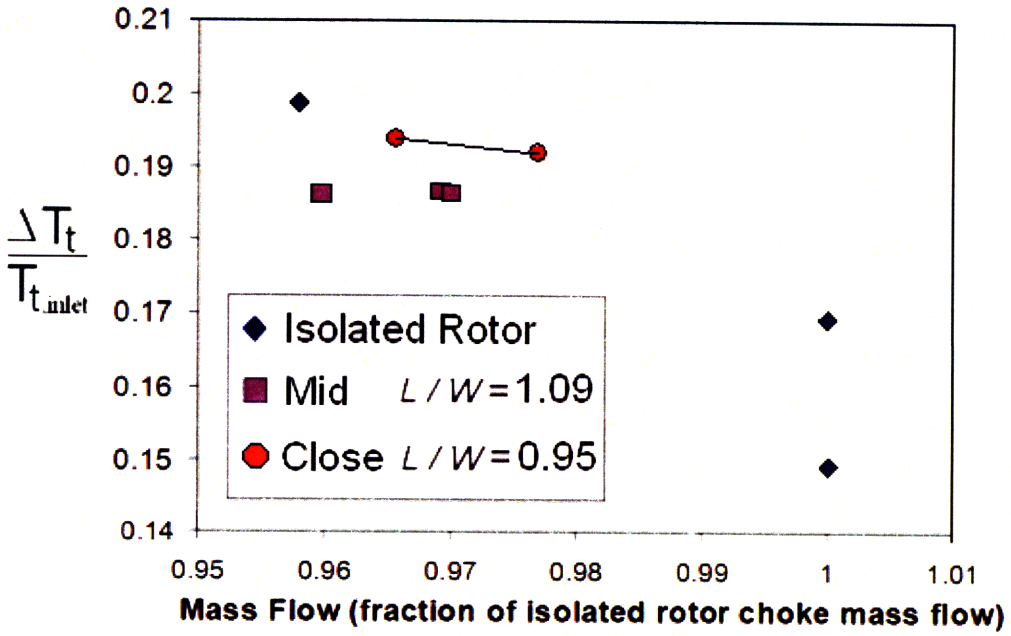

Figure 4.2: Stagnation temperature rise vs. mass flow for the isolated rotor, and the Mid and Close geometries.

flow of 0.97.

The steady-state analysis model and the B_3 parameter can thus be used not only to explain the effect of changes in wake phasing but also to provide guidelines for wake phase to have a beneficial impact on work input.

4.2 Increase of Sensitivity to Wake Phasing Due to Increased Vane Count

When the vane count of the upstream blade row is increased, the potential for change in performance due to change in wake phase is also increased. To show this, the numerical experiment described in the Section 4.1 was repeated for a geometry in which the number of inlet guide vanes was increased by 50%. Thus the geometries now had an IGV-to-rotor ratio of one-to-one (to form the Mid_{1-1} and the $Close_{1-1}$ configurations) compared to an IGV-to-rotor ratio of two-to-three for the original geometry. The purpose of increasing

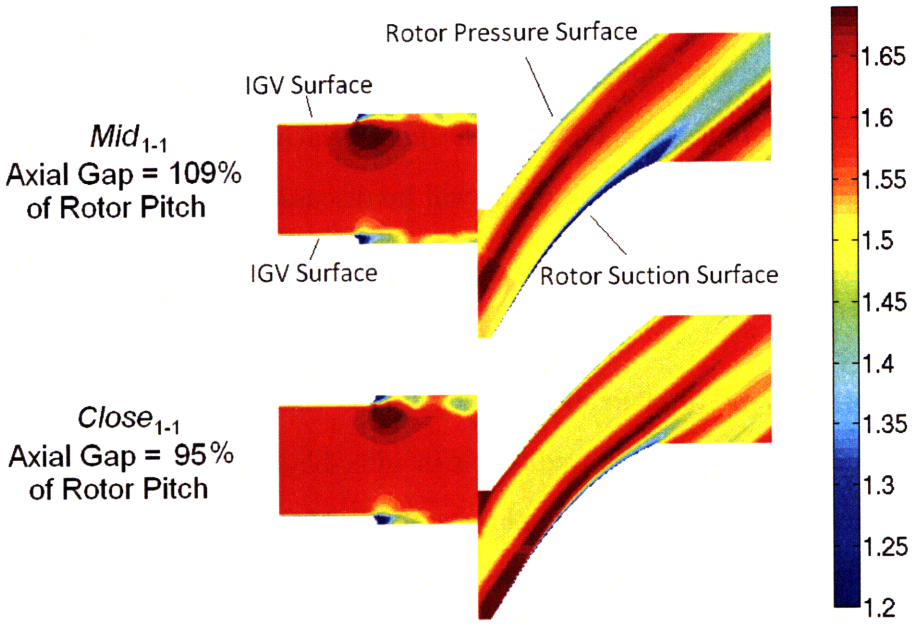

Figure 4.3: Time-mean relative stagnation pressure contours for Mid_{1-1} and $Close_{1-1}$ geometries.

the number of IGV's was to increase the number of wake vortices convecting through the rotor passage. According to the ideas described in Chapter 3, this will result in a greater amplitude of stratification than in the previous calculations, because the time-mean vorticity due to the wake vortices will be greater. From Equation 3.2, the increase in time-mean vorticity is associated with an increase in stagnation pressure gradient, and a greater amplitude of time-mean relative stagnation pressure leads to a greater variation in the rotor boundary layer edge velocity as a function of phase. Therefore, the sensitivity of the rotor work input on the wake phase is greater with increased vane count.

Figure 4.3 shows the time-mean relative stagnation pressure contours for the Mid_{1-1} and $Close_{1-1}$ geometries. The latter spacing results in a smaller suction side displacement thickness, as was the case in section 4.1. At a fixed corrected massflow, the work input and efficiency of the $Close_{1-1}$ spacing was 6.8% and 0.9 points higher, respectively, compared to the Mid_{1-1} spacing. The work input and efficiency are more sensitive to

the phase for the configurations with greater number of vanes, i.e., the same change in phase resulted in a greater change in work input and efficiency when the vane count was increased. The connection between the inlet relative stagnation pressure profile amplitude and the variation in work input will be discussed in Chapter 5.

4.3 Summary

If a reduction in vane-rotor axial gap is chosen so that the wake phase is improved significantly, it is possible for the reduction in inter-bladerow spacing to increase the rotor work input. The Close spacing configuration had an inter-bladerow spacing 13% smaller than the Mid spacing, yet resulted in a work input 4% larger than the Mid configuration. When the vane count was increased by 50%, the increase in rotor work input due to the reduction from Mid to Close spacing was 6.8%.

Chapter 5

Scaling Parameters for the Effects of Wake Phasing

5.1 Approach to Determine Scaling of Wake Phasing Effects to Flow Parameters

The focus of this chapter is on establishing how the phase-related dependence on work input scales with flow parameters. To accomplish this a series of numerical computations was performed to determine the influence of (i) inlet relative Mach number and (ii) amplitude of the relative stagnation pressure profile on the sensitivity of the rotor work input to wake phasing. Following on from the results shown so far, steady calculations were used. The input was an inlet flow of nonuniform stagnation pressure. The output that is reported here is the tangential force. All quantities reported are in the rotor relative frame. The position of the inlet profile was shifted to define the relationship between tangential force and pitchwise profile position. A fractional change in tangential force translates to an equal fractional change in work input. A range of inlet Mach numbers and amplitudes of inlet stagnation pressure nonuniformity have been assessed to provide the scaling information.

MISES [23] was used for these parametric studies due to the short convergence time required for the steady calculations and the greater control in maintaining a constant inlet corrected massflow at which to compare different cases. The stagnation pressure profile was nonuniform but the stagnation temperature was uniform.

A generic blade geometry and stagnation pressure profile were used, so the blade geometry and inlet profile were not exact duplicates of those from the SMI calculations. However, the effect being studied is not dependent upon the specific blade characteristics

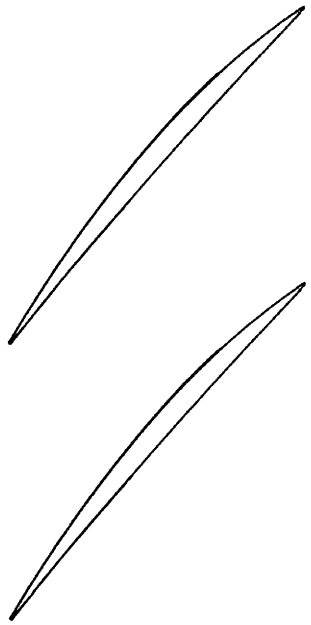

Figure 5.1: DFVLR transonic cascade used in parametric calculations. The Reynolds number was 1.5×10^6.

and therefore the applicability of the results is not inhibited. Figure 5.1 shows the geometry used, which was a section of a transonic cascade designed by DFVLR (German Research and Test Institute for Air and Space Research) [24]. The DFVLR cascade geometry was chosen as a represenative transonic cascade geometry, and one already present within MISES with extensive testing.

The stagnation pressure profile used was also generic. Minor modifications to MISES were done in order to allow for the input of a nonuniform stagnation pressure at the domain inlet (see Appendix C). The profile shape consisted of two hyperbolic tangent curves joined together, as in the sample profile shown (Figure 5.2). The profile is periodic with a wavelength equal to the rotor pitch, characteristic of time-mean relative stagnation pressure profiles from phase-locked vortices. The results should thus be applicable for the range of Mach numbers and amplitudes shown. Throughout the paper, pitch location of 0 refers to the rotor pressure surface, and pitch location of 1 refers to the suction surface.

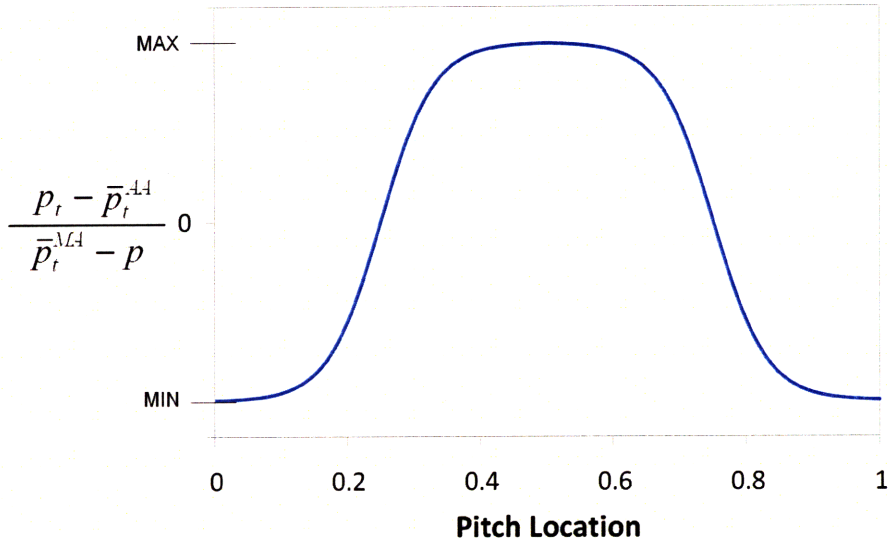

Figure 5.2: Inlet nominal stagnation pressure nonuniformity (based on the time-mean of the unsteady computations).

The inlet Mach number and stagnation quantities, as well as the outlet static pressure boundary conditions were specified in the MISES setup. The outlet static pressure was adjusted until the desired tangent of the inlet flow angle, based on mixed-out conditions, of 1.63 was achieved within a value of 0.005. This corresponded to the design flow coefficient. The variation of 0.005 was determined to cause variations in the work input that were an order of magnitude less than the work input change caused by the variation in wake phase, so the flow angle at the inlet is controlled precisely enough that changes in the inlet flow angle do not significantly affect the results. With the inlet angle fixed, the inlet profile is identical for the different cases, except for the pitchwise position of the profile relative to the blade. The nondimensional parameters used, and the results of this parametric study, are described in the following section.

5.2 Parametric Study

To describe the amplitude of the stagnation pressure nonuniformity, the following nondimensional stagnation pressure parameter (DPT) is used:

$$DPT = \left(\frac{p_{t,max} - p_{t,min}}{\overline{p}_t^{MA} - p} \right)_{inlet}. \tag{5.1}$$

The DPT parameter is the peak to peak difference in stagnation pressure at the inlet, divided by the inlet dynamic pressure.

The nondimensional tangential force coefficient is the Delta Force Coefficient (DFC), defined as

$$DFC = \frac{F_\theta - \overline{F}_\theta}{\left(\overline{p}_t^{MA} - p\right)_{inlet}}. \tag{5.2}$$

In Eqn. 5.2, F_θ is the tangential force on the blade per unit flow area corresponding to the current inlet profile and $\overline{F}_\theta$ is the tangential force per unit flow area calculated when a uniform inlet profile is used. For a uniform flow the value of DFC is zero.

Figure 5.3 shows the tangential blade force as a function of the pitchwise location of the stagnation pressure profile for three different data sets. Each data set in Figure 5.3 corresponds to a different value of inlet (DPT/Nominal DPT), with the nominal value of DPT chosen to equal that measured in the MSUTurbo calculations, 0.16. One data set has a DPT equal to the nominal value, one an inlet value of DPT twice the nominal value, and the third a DPT half the nominal value. All three data sets have an inlet relative Mach number of 0.5. The trends are consistent with the results from the MSUTurbo calculations in that the greatest tangential force is obtained when fluid with the highest stagnation pressure encases the blade. All the data collapses well, implying that the change in work input due to change in wake phase is almost directly proportional to the inlet value of DPT.

Figure 5.4 shows the tangential force on the blade row as a function of the pitchwise position of the inlet stagnation pressure profile for five different data sets. Each data set represents a different inlet Mach number. A Prandtl-Glauert compressibility correction has been applied to the values of Delta Force Coefficient. With this correction, the subsonic data sets collapse, showing that compressibility increases the sensitivity of the

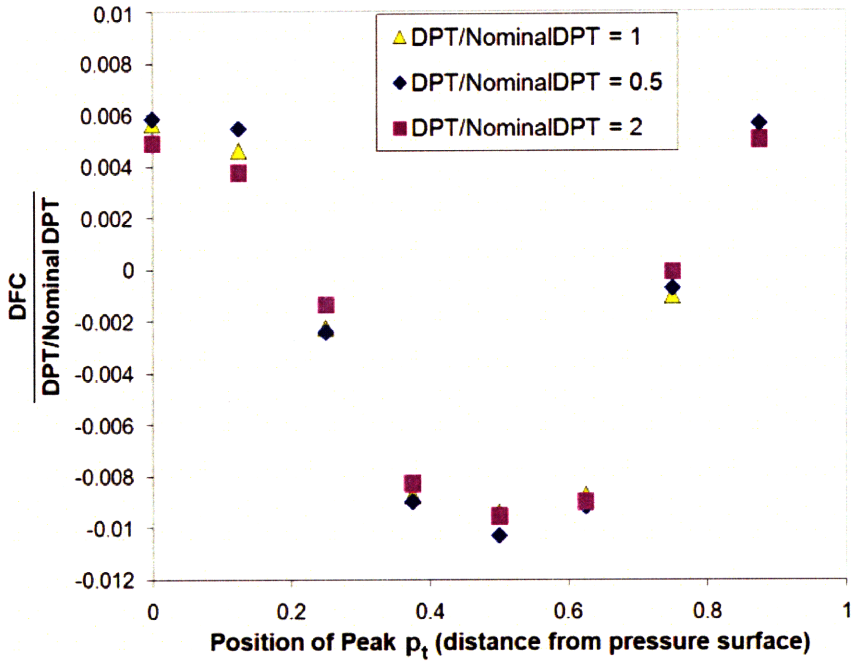

Figure 5.3: Circumferential force variation (DFC) vs. pitchwise position of inlet stagnation pressure profile for different amplitudes of inlet nonuniformity. All data sets have an inlet relative Mach number of 0.5.

tangential force to the wake phase, and that this difference can be estimated using a compressibility correction of $1/\sqrt{1-M^2}$. The supersonic data set(M = 1.15) does not collapse with the other sets. This may be due to mitigation of the amplitude of the stagnation pressure profile that occurs when the flow passes through the shock.

In addition to showing the scaling, the calculations confirm that the steady model captures the effect of changes in wake phasing, in that the results in Figure 5.3 are applicable to the unsteady calculations described earlier for the Far and Mid configurations. The Far case corresponds to a peak stagnation pressure position of approximately 0.2, and the Mid case to 0.55. Figure 5.3 shows that the difference between DFC values for the Far and Mid cases should be approximately 0.008 (the difference in ordinates between abscissas of 0.2 and 0.55). The actual difference in DFC between the Far and Mid configurations in the unsteady Turbo calculations was 0.0089, close to the estimate.

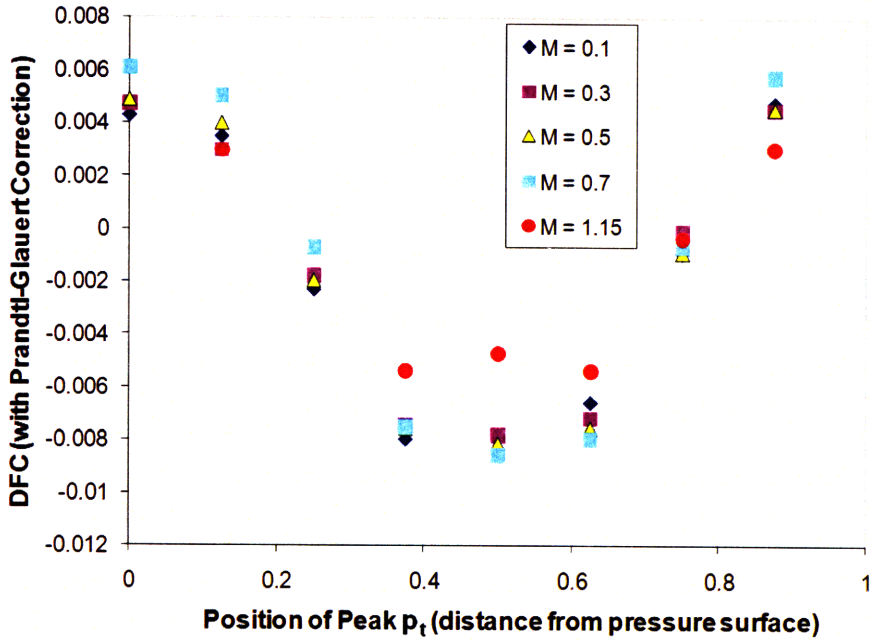

Figure 5.4: Circumferential force variation (DFC) vs. pitchwise position of inlet stagnation pressure profile for different rotor inlet Mach numbers. All data sets have a DPT of 0.16 at the domain inlet.

5.3 Effect of Vane Trailing Edge Thickness

For wake phasing to have a measurable impact on the rotor performance the vane must shed counter-rotating vortices that are phase-locked to the rotor and create a level of time-mean relative stagnation pressure nonuniformity that is of engineering interest. For this to occur the rotor-induced static pressure field must couple strongly to the upstream vane flow. There are geometric requirements for such a wake to exist, because the counter-rotating vortices shed behind a vane with thick trailing edge have been found to have greater circulation than those for the same shock but a thin trailing edge. To quantify how the magnitude of the wake phasing effect depends on the vane geometry, calculations were carried out in which the axial IGV row was replaced with a vane row with thin trailing edge. The thin-edged row employed was a deswirler row designed to be used in the SMI facility with a swirling flow upstream of the vane [25]. The flow upstream of the deswirler has a swirl angle of 29 degrees, with the deswirler turning it

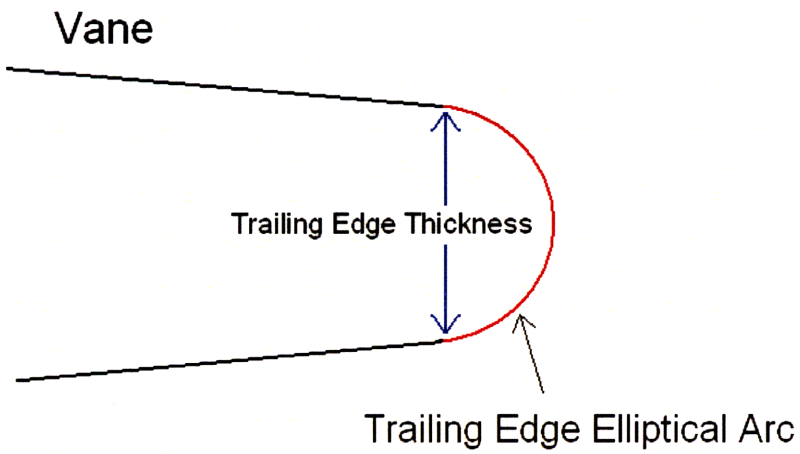

Figure 5.5: Trailing edge thickness measurement illustration. The thickness of the vane trailing edge is measured at a chordwise location where the elliptical curve forming the trailing edge begins.

to the axial direction.

The deswirler has a much thinner trailing edge than the original axial guide vanes (0.0155 versus 0.111 of the rotor pitch, respectively). The trailing edge of the vanes are essentially elliptical arcs, and the trailing edge thickness was measured as the thickness of the vane (normal to the camber line) at the axial location where this elliptical curve starts. Figure 5.5 illustrates the "trailing edge thickness". In accord with the mechanism postulated by Gorrell et al. [6] the magnitude of the shed circulation is greatly reduced with the reduction of the vane trailing edge thickness. Figure 5.6, which can be compared with Figure 2.4, shows the deswirler wake and its passage through the rotor. It can be seen that there are qualitative differences between the vortex configurations and strengths in the two figures. In Figure 5.6, the phase-locked regions of high vorticity that were present within the rotor passages in Figure 2.4 are absent.

Figure 5.6 shows the point qualitatively, but Figure 5.7 and Figure 5.8 quantitatively illustrate the effect of trailing edge thickness on the amplitude of the rotor inlet relative stagnation pressure nonuniformity. Figure 5.7 shows the profile of time-mean relative stagnation pressure for the IGV-rotor and the deswirler-rotor calculations, both at Far spacing. The nonuniformity corresponding to the deswirler-rotor geometry is substan-

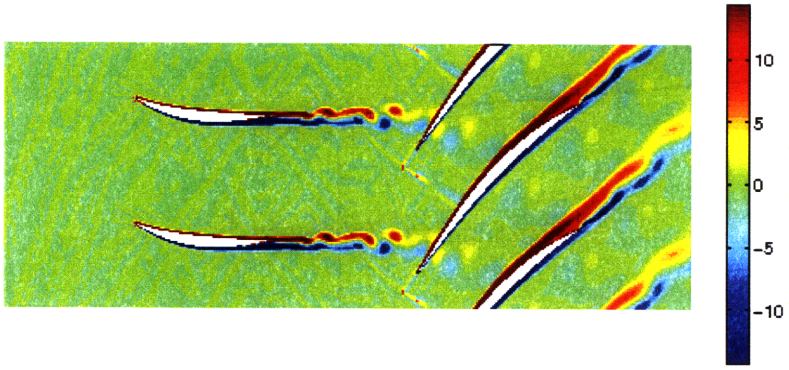

Figure 5.6: Vorticity contours for SMI deswirler-rotor geometry. The phase-locked wake vortices are far weaker than those shown in figure 2.4.

tially smaller than that for the thick IGV-rotor geometry.

The difference between the maximum and minimum values of each profile in Figure 5.7, along with two other cases, are plotted in Figure 5.8, as a function of the ratio of vane thickness to vane pitch. The four points correspond to calculations with a (i) flat plate IGV (zero thickness), (ii) and (iii) two thick IGVs with different pitchwise spacings, and (iv) the thin-edged deswirler. All the calculations are carried out at the same axial spacing from vane trailing edge to rotor leading edge of 1.22 times the rotor pitch. The number of blades in the vane row differs between the cases, while the rotor geometry is the same for each configuration; so the vane-to-rotor count varies between the cases. The configuration using the deswirler and the higher solidity inlet guide vane configurations all have a vane-to-rotor ratio of one-to-one. The cases using the flat plate and the lower solidity IGV row have a vane-to-rotor ratio of two-to-three.

For the flat plate there is an order of magnitude difference with the thick IGV in the time-mean relative stagnation pressure nonuniformity presented to the rotor. The deswirler creates a larger nonuniformity, but it is still a factor of five or so below that of the thick IGV. The calculations imply that the amplitude of the time-mean relative stagnation pressure nonuniformity at the rotor inlet is roughly proportional to the vane trailing edge thickness divided by the vane pitch, although there may be additional

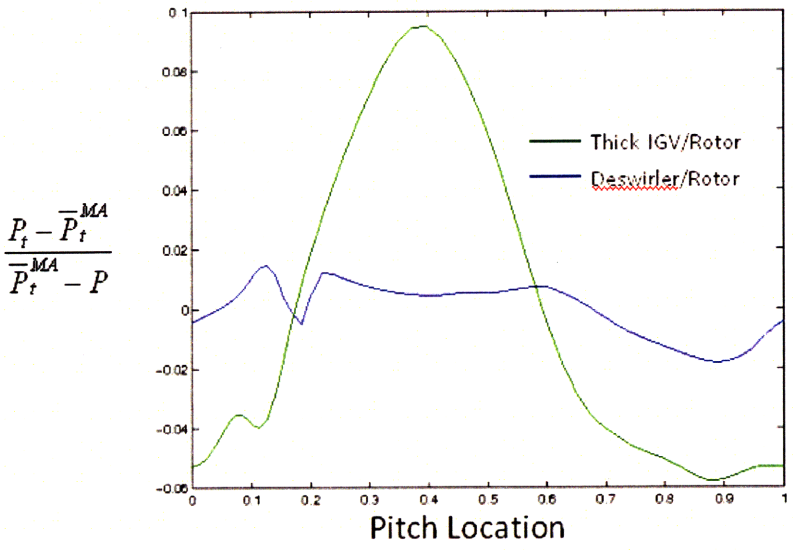

Figure 5.7: Time-mean relative stagnation pressure profile 10% of the rotor chord upstream of the rotor for the thick IGV-rotor and the deswirler-rotor configurations.

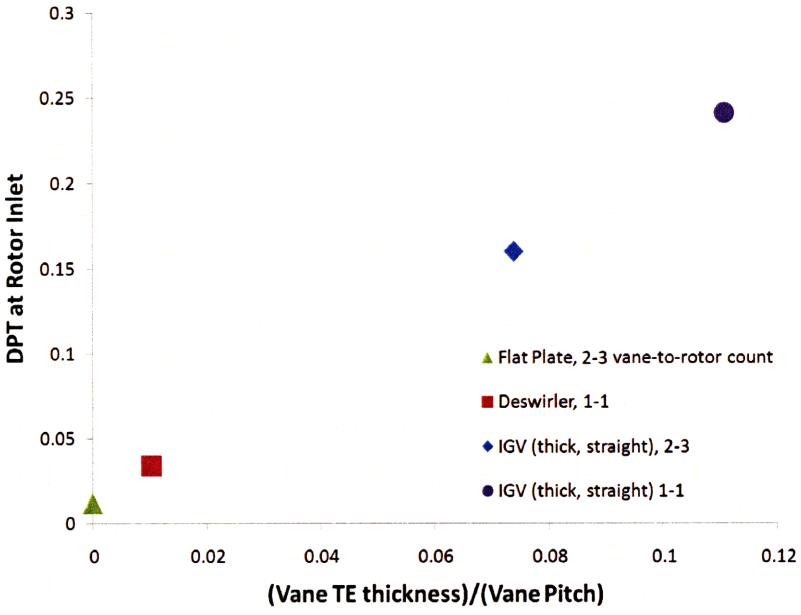

Figure 5.8: Amplitude of stagnation pressure profile (DPT) vs. vane trailing edge thickness/vane pitch. Inter-bladerow spacing of L/W=1.22 used for all data points in the figure.

parametric dependencies. Examination of high-fidelity three-dimensional calculations of a swirler/deswirler/rotor geometry performed by List [25] also indicates that a small ratio of trailing edge thickness to vane pitch leads to a reduced time-averaged relative stagnation pressure nonuniformity.

5.4 Effect of Vane Loading on Wake Phasing

It is not suggested that all the parametric dependencies relevant to the creation of a time-mean relative stagnation pressure nonuniformity have been examined in this work. However, the parametric dependencies presented are the primary factors in determining the value of DPT. Two additional data points with increased aerodynamic loading were obtained in order to assess whether the value of DPT for the flow entering the rotor is independent of the loading on the upstream vane row. To increase the loading on the upstream vane row, the flow angle upstream of the deswirler in the deswirler-rotor configuration was increased.

Figure 5.9 shows contour plots of vorticity for the deswirler-rotor case. Each plot corresponds to a different vane incidence angle. In Figure 5.9(a) the incidence on the deswirler is at the design, or nominal, value, referred to as N degrees. In Figure 5.9(b), the flow angle upstream of the deswirler is altered so the incidence angle is N+3 degrees. In Figure 5.9(c) the incidence angle is N+5 degrees. The thickness of the region of vorticity directly adjacent to the suction surface indicates that in both cases of increased vane incidence angle, the boundary layer is larger than the nominal case. The displacement thickness is 22% larger at N+3 degrees incidence and 115% larger at N+5 degrees than for the nominal situation. Even at the increased vane incidences, however, strong discrete vortices such as those observed in Figure 2.4 are not evident in the vane wake.

The data points for the deswirler-rotor configurations with increased loading are added to the plot of DPT versus the ratio of trailing edge thickness to vane pitch from Figure 5.8, and the result is given as Figure 5.10. The data points corresponding to the

deswirler-rotor cases are represented in Figure 5.10 by the three square symbols at the x-value of 0.0103. The additional points are closely clustered, indicating that the vane loading, and therefore vane boundary layer thickness, has only a minimal influence on the DPT, since the DPT value is still more than five times smaller than with the thick IGV. The difference in DPT between the deswirler-rotor with N degrees incidence and the case with N+5 degrees incidence is 0.0056, a difference of 17 percent of the nominal value.

As further illustration that the phase-locked vorticity shed by the deswirler vane is small compared to the case with the thick IGV, Figure 5.11 shows the time histories for the flux of shed vorticity. The measurement location was a constant axial plane midway between the vane trailing edge and the rotor leading edge. Three data sets, all with axial spacing of 1.22 times the rotor pitch and vane-to-rotor counts of one-to-one, are included in Figure 5.11. They are i) the IGV-rotor case, ii) the deswirler-rotor case with the deswirler at nominal incidence, and iii) the deswirler-rotor case with the deswirler at N+5 degrees incidence. The ordinate is the time-instantaneous flux of vorticity through the measurement plane, normalized by the maximum flux that is measured in the IGV-rotor case. The abscissa of the plot is the rotor blade passing number. The magnitude for the signals representing the deswirler-rotor cases are all an order of magnitude smaller than that of the IGV-rotor case. This shows that even when the deswirler is highly-loaded, the magnitude of the phase-locked vorticity shed is small.

5.5 Application to a Three-Dimensional Geometry

We have shown that the effect of the wake phase on the work input per unit span at any given span of the flow can be determined by calculating the amplitude and phase of the time-averaged flow profile at the given span, and using the scaling correlations described in section 5.2. Thus, if the three-dimensional flow is divided into several spanwise sections and then the results of the wake phase analyses from the different spans

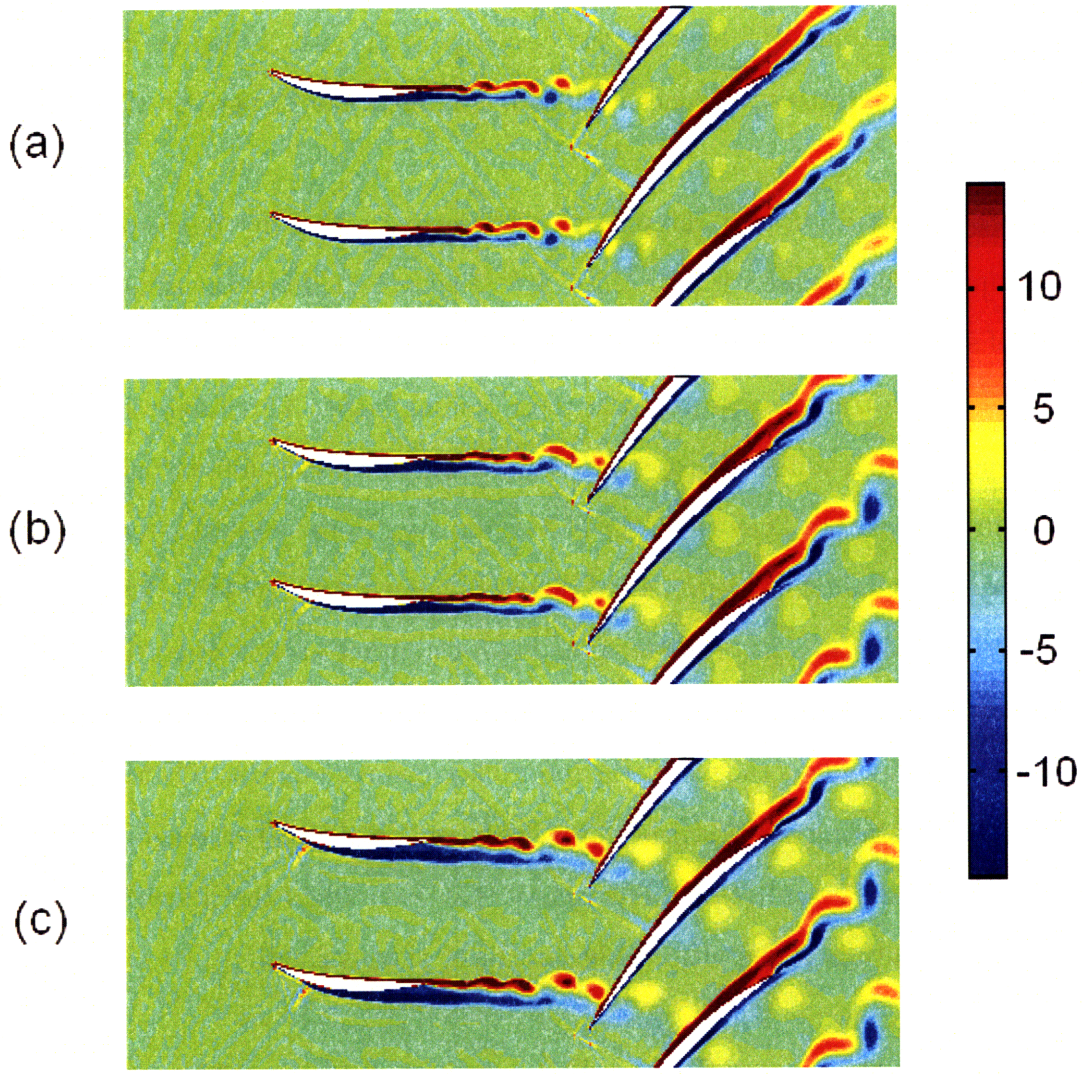

Figure 5.9: Vorticity contours for SMI deswirler-rotor geometry, at three different vane inlet incidences[(a) is the nominal (N) vane incidence, (b) has incidence of N+3 degrees, and (c) N+5 degrees]. The phase-locked wake vortices are far weaker than those shown in Figure 2.4, even when the boundary layer is thick.

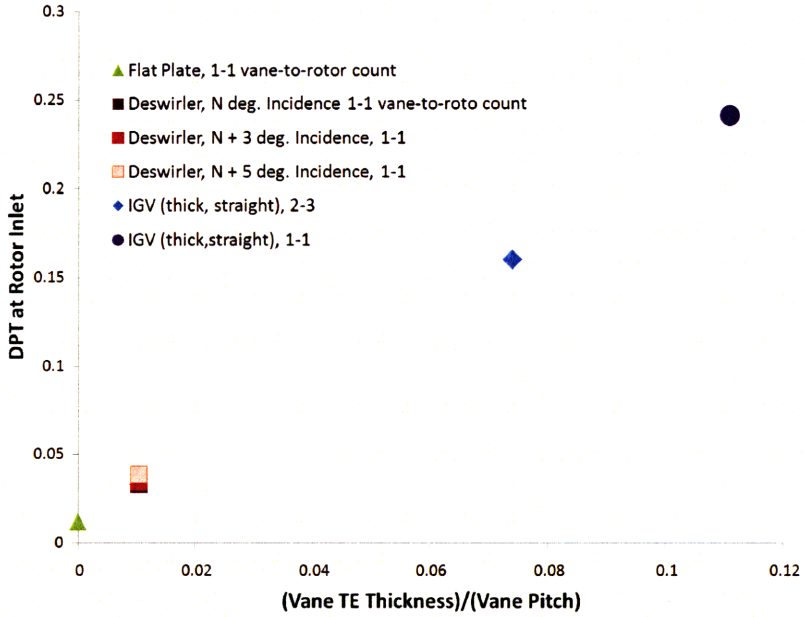

Figure 5.10: Amplitude of relative stagnation pressure profile (DPT) vs. vane trailing edge thickness/vane pitch. The same inter-bladerow spacing (L/W=1.22) was used for all data points in this plot. Three different vane loadings for the deswirler-rotor case are included.

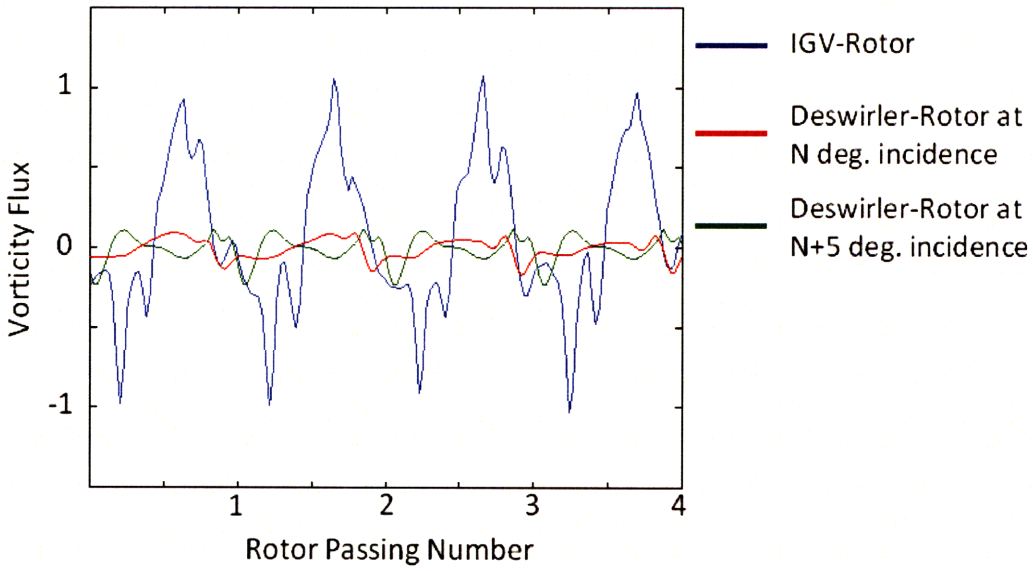

Figure 5.11: Flux of vorticity through a plane at constant axial position vs. time. The measurement plane is midway between the vane trailing edge and the rotor leading edge. The same inter-bladerow spacing (L/W=1.22) and the same vane-to-rotor count (one-to-one) were used for all three data sets. The vorticity flux is normalized by the maximum vorticity flux in the IGV-rotor case, and the time is normalized by the rotor passing period.

are weighted appropriately, the total effect of the wake phasing on the three-dimensional geometry can also be estimated. Since the ordinate in Figure 5.3 is the force per unit flow area normalized by the inlet dynamic pressure, the appropriate weighting of the force per unit span at the different span locations is the inlet relative dynamic pressure times the pitch at that span location. Since the pitch is proportional to the radius, the weighting factor is

$$WeightingFactor = \left(\overline{p}_t'^{MA} - p\right)_{span} r. \tag{5.3}$$

For the three-dimensional SMI geometry with inter-bladerow spacing A, the potential for change in work input per unit span due to change in wake phase can be as high as 9%, depending on which spanwise location is being considered. However, since the wake phase at some spanwise locations can be beneficial while the wake phase at other spanwise locations are detrimental, the net potential for change in work input over the entire span is less. Figure 5.12 shows the relative stagnation pressure contours at the 30% span and the 90% span. At the lower span, the peak relative stagnation pressure (at that particular span) is adjacent to the pressure surface of the blade. At the higher span, the peak relative stagnation pressure is near the midpitch of the rotor passage. Note that the relative stagnation pressures at the lower spans are generally less than those at higher spans because of the slower blade speed.

Figure 5.13 is a plot of the wake phase vs. span. At a given span, the wake phase is quantified in the plot by the pitchwise position of the fluid with highest relative stagnation pressure at the rotor inlet. For the abscissa, a value of 0 corresponds to the hub and a value of 1 corresponds to the casing. The data in Figure 5.13 shows that the phase varies approximately linearly with span.

Based on the numerical results from the middle 80% span of the Stage Matching Investigation Rig, a stacked two-dimensional analysis gives an estimate that changes in wake phasing can be responsible for a 1.2% change in the work input of the three-

dimensional SMI rotor. It may be possible, however, to design a compressor geometry for which the wake phase is beneficial across a larger portion of the span, increasing the potential benefit.

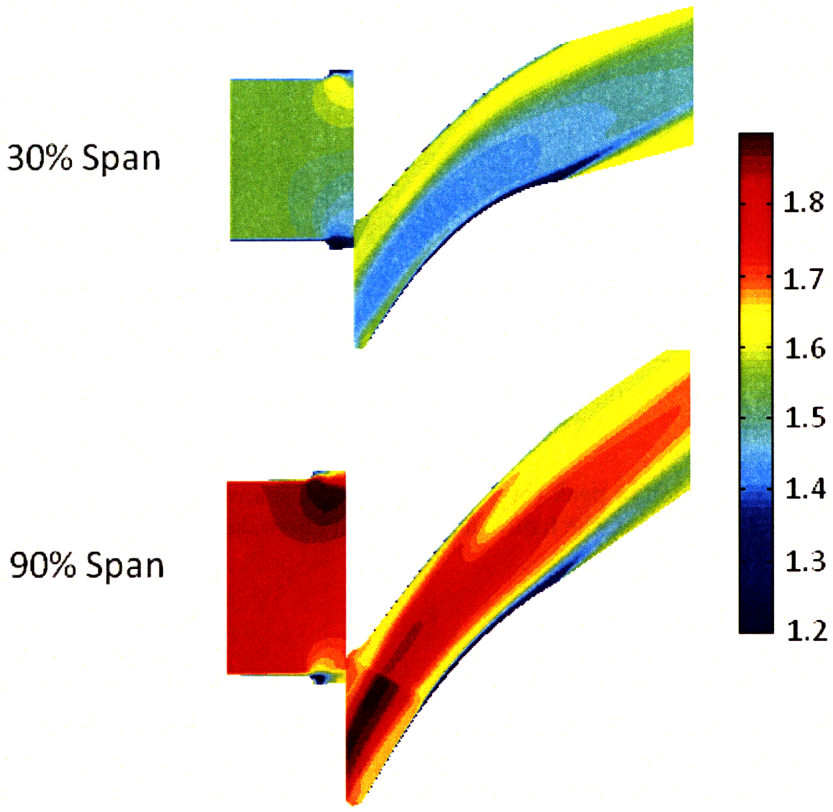

Figure 5.12: The contours of time-mean relative stagnation pressure for the SMI spacing A configuration. The contours shown are at 30% and 90% span to illustrate how the phase varies with span.

5.6 Summary

Parametric studies reveal that the effect of wake phasing on the rotor work input is proportional to the magnitude of DPT at the inlet. The effects of wake phasing increase with inlet relative Mach number, and this increase in sensitivity is captured by a Prandtl-Glauert compressibility correction.

The DPT for the vane wake is dependent on the vane geometry. DPT varies linearly with the ratio of the vane trailing edge thickness to the vane pitch, and is roughly

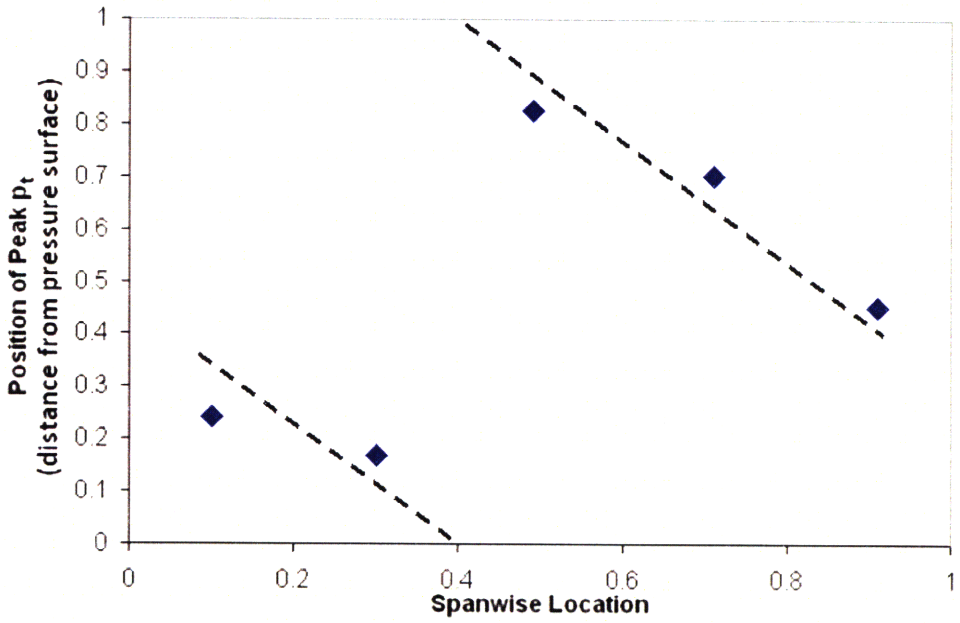

Figure 5.13: Pitchwise location of peak total pressure vs. the spanwise location for the SMI geometry with spacing A. The dotted line in the figure indicates that the wake phase varies approximately linear with span.

independent of the vane loading.

The effect of wake phasing on a three-dimensional compressor geometry can be determined by treating the three-dimensional flowfield as a series of two dimensional flowfields stacked radially. The effect of wake phasing at each spanwise section can be appropriately weighted to estimate the overall influence on work input.

Chapter 6

Three-Dimensional Effects of Wake Phasing

6.1 Impact of Tip Clearance Flow on Rotor Blockage

The discussions so far have been about effects that can be viewed as two-dimensional. There are, however, consequences of the creation of a stratified relative stagnation pressure field which are three-dimensional in nature and qualitatively different from those already mentioned. A specific example described in this chapter is the effect that wake phasing can have on tip clearance flow and hence on maximum pressure rise capability of a compressor.

The positioning of the wake phase in the tip clearance region can affect peak pressure rise capability, and possibly operating range. The link is through the clearance flow, a major contributor to rotor exit blockage and hence to the pressure rise limitation, and its sensitivity to relative stagnation pressure stratification. As described by Khalid [26], increasing the relative stagnation pressure of the tip clearance vortex core decreases the blockage at the rotor exit, thus increasing the pressure rise capability. If the relative stagnation pressure profile can be positioned such that the high stagnation pressure fluid forms the core of the clearance vortex, flow stratification offers a potential to reduce the blockage and increase the peak pressure rise.

Khalid showed that the physical mechanism is usefully modeled as a velocity defect in an adverse pressure gradient, as depicted in Figure 6.1a. The area and depth of the downstream velocity defect depends on the rate and magnitude of the pressure rise. The value of $C_{p,s}$ is used here to denote the static pressure rise from inlet to exit, divided by the freestream inlet dynamic pressure. The deficit in stagnation pressure can be represented by

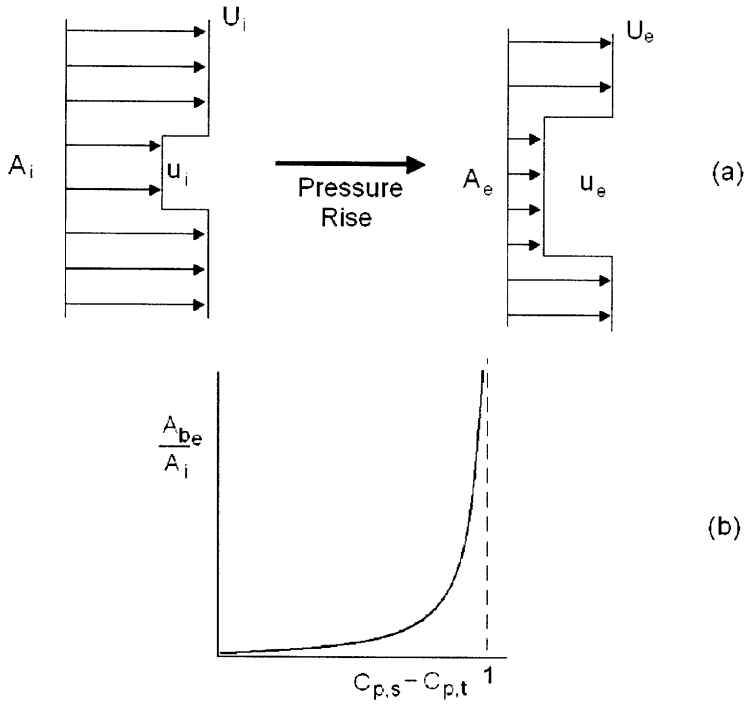

Figure 6.1: Depiction of velocity defect in a flow through an adverse pressure gradient and asymptote in blockage at critical loading factor. A_i and A_e represent the area of the velocity defect before and after passing through the adverse pressure gradient, respectively. $A_{b,e}$ is the displacement thickness associated with the velocity defect of the fluid after passing through the pressure gradient.

$$C_{p,t} = \frac{p_{t,defect} - p_{t,free-stream}}{q_{i,free-stream}} \tag{6.1}$$

From Bernoulli's equation the velocity in the defect goes to zero and there is an asymptote in blockage when the $(C_{p,s} - C_{p,t}) = 1$. The region of rapid increase in blockage has been linked with a drop in pressure rise and the onset of instability [26]. This behavior is depicted graphically in Figure 6.1b, which shows a plot of $A_{b,e}/A_i$ as a function of $(C_{p,s} - C_{p,t})$, where $A_{b,e}$ is the displacement thickness of the wake at the downstream station, defined below in Equation 6.2.

$$A_{b,e} = \left(1 - \frac{u_e}{U_e}\right) \cdot A_e \tag{6.2}$$

If the time-averaged nonuniformity in relative stagnation pressure in the rotor ref-

erence frame enables an increase in the relative stagnation pressure of the fluid which makes up the tip clearance vortex core, for a given static pressure rise through the blade passage, the parameter $(C_{p,s} - C_{p,t})$ will be decreased. Higher pressure rise can thus be achieved through the blade passage before the asymptotic limit of loading parameter is reached.

6.2 Numerical Test Assessing Effects of Wake Phasing on Tip Clearance Flow

A similar procedure to that used to create the nonuniform inlet profile in the two-dimensional case was used for the three-dimensional simulations. A uniform inlet condition was used as the base flow, and pre-processing tools were used to change this base flow to give the appropriate stagnation pressure profile at the inlet. Thus, the time-mean effect of the wake phasing near the casing was modeled as a steady inlet profile with a pitchwise nonuniformity in relative stagnation pressure near the tip, similar to the procedure described in section 3.3. Two-dimensional model calculations have already shown that this approximation captures the most important aspects of the wake phasing phenomenon.

For the three-dimensional calculations, the outer 15% of the inlet flow was stratified in relative stagnation pressure, using a value of nonuniformity (DPT) approximately three times that observed downstream of the vanes in the SMI geometry. These calculations have been deliberately abstracted compared to the actual situation in that the profile of rotor inlet stagnation pressure does not account for the radial variation that exists near the casing, and the steady calculations do not capture unsteady perturbations in tip vortex motion. The point of the computations in this section, however, are more qualitative than those in the rest of the thesis with the objective of evaluating the plausibility of the idea that wake phasing can affect the tip clearance flow.

Figure 6.2 shows the relative stagnation pressure contours at the inlet flow plane for

one of the test cases. The nonuniformity was shifted to evaluate the rotor performance sensitivity to the pitchwise position. The position of the stratification shown in Figure 6.2 is referred to as "position 1". A shift of one-quarter pitch in the direction of rotor rotation puts the profile at "position 4"; a second shift of a quarter pitch gives "position 3", and another quarter-pitch shift gives "position 2." The inlet profile below 85% span is close to uniform, although the influence of the rotor shock at the domain inlet produces some small variation in the pitchwise direction. The imposed variation in relative stagnation pressure in the tip region was more than five times greater than the variation due to the rotor shock.

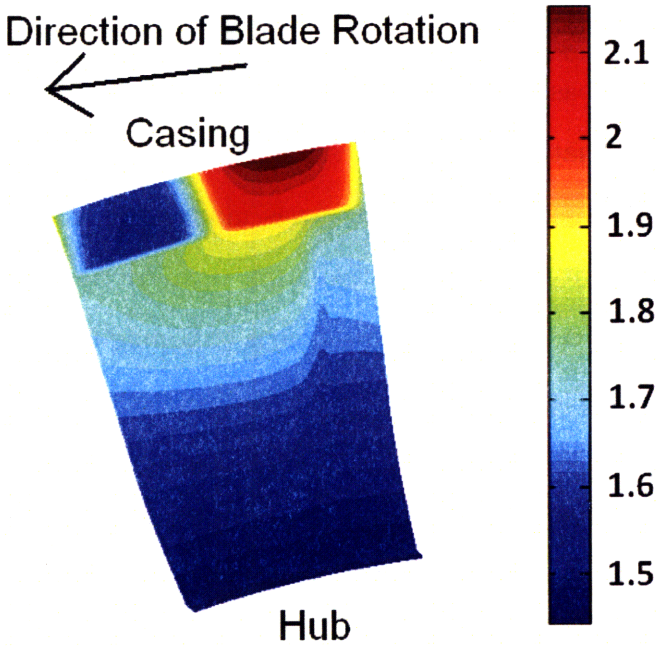

Figure 6.2: Relative stagnation pressure at domain inlet for test case (stratified inlet "position 1").

6.3 Results of Tip Clearance Experiments

The results from computations with different relative stagnation pressure peak positions are given in Figure 6.3. The ordinate is the rotor total-to-static pressure rise

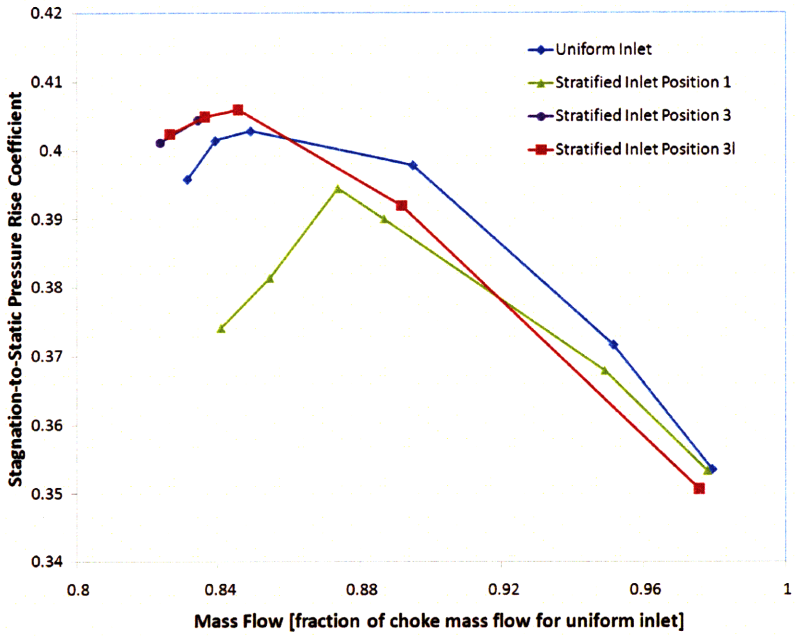

Figure 6.3: Stagnation-to-static pressure rise coefficient vs. mass flow for the three-dimensional calculations. The results from the uniform inlet case and stratified inlet position 1 and position 3 cases are shown.

coefficient (exit static pressure minus inlet absolute stagnation pressure, normalized by the mass-averaged relative inlet dynamic pressure, as shown in Eqn. 6.3).

$$C_{p,t-s} = \frac{p_2 - p_{t,1}}{q'_1} \tag{6.3}$$

The abscissa is the corrected mass flow normalized by the choke corrected mass flow for the case with uniform inlet. The data set for position 1 is the inlet profile position that resulted in the worst near stall performance in terms of numerical stall flow coefficient and stagnation-to-static pressure rise coefficient, while position 3 resulted in the best near stall performance. For these calculations, the flow coefficient at which the rotor exhibited numerical stall differed by 2.1%, and the pressure rise coefficient at near stall conditions varied by 6.8%.

The reason for the performance change is the difference in tip clearance related blockage that accompanies the change in profile position. The effective flow area at the rotor

exit varied by 3.3%, depending on the inlet profile. An additional calculation result is denoted by "position 3l", which refers to the same inlet circumferential profile as position 3, but with stratification only present in the outer 10% of the span, rather than the outer 15%. The difference between the results obtained with "position 3l" and "position 3" inlet profiles was small, with only a 0.3% change in both the stall flow coefficient and pressure rise coefficient at stall.

As a reference for where the high stagnation fluid should be located for best performance, Figure 6.4 shows the relative stagnation pressure for the flow at the blade tip span for the stratified inlet position 3. At a mass flow near stall, this inlet position results in a flowfield in which the fluid with highest relative stagnation pressure impinges on the forward half of the pressure side of the rotor blade, which is where the tip clearance vortex is drawn from. The implication is that if wake phasing near the casing is significant, the phase can be tailored to produce a time-averaged profile in relative stagnation pressure that produces a higher total-to-static pressure rise at near stall conditions than that of the uniform inlet flow. The following section describes in more detail the link between the change in performance and the change in blockage due to the tip clearance flow.

6.4 Changes in Blockage and the Corresponding Effects on Performance

A change in rotor exit blockage changes the effective flow area at the rotor exit and therefore the pressure rise capability [26, 27]. For example, the blockage at near stall conditions with uniform inlet was less than that of stratified inlet position 1. This can be seen from Figures 6.5a and 6.5b, which depict the relative stagnation pressure at the rotor exit plane for the uniform inlet and stratified inlet position 1, respectively. The region of low relative stagnation pressure near the casing is the blockage due to the tip clearance flow. For the stratified inlet position 1 configuration, the region of low relative

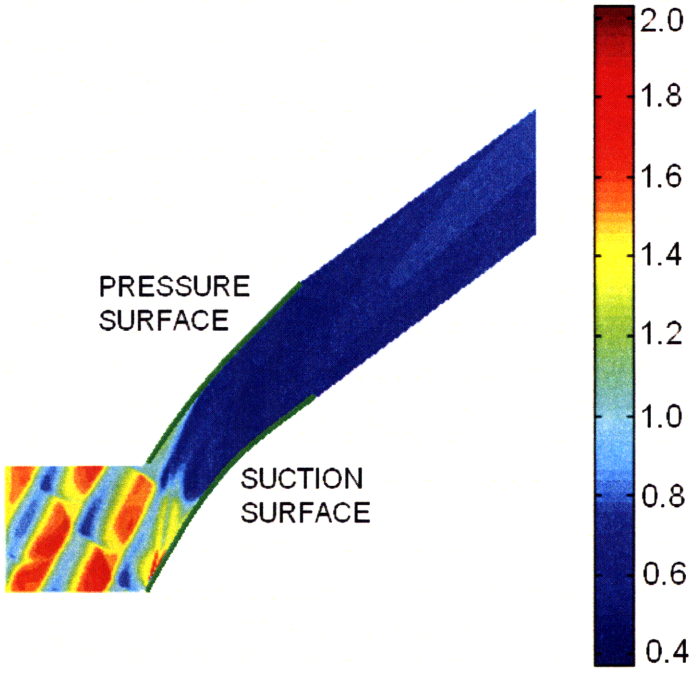

Figure 6.4: Relative stagnation pressure contours at the blade tip span for the stratified inlet position 3, at a mass flow of 0.826.

stagnation pressure, and therefore blockage, is more severe than in the uniform inlet configuration.

Murray [28] described a method that could be used to compare the effective area of two flows. The difference in effective flow area is

$$\Delta A_{eff} = \Delta \left(\frac{\dot{m} \int d\dot{m}}{\int \rho W_{TF} d\dot{m}} \right), \tag{6.4}$$

where $\dot{m}$ is the mass flow, W_{TF} is the relative throughflow velocity, and the value of this metric is calculated on an $r - \theta$ plane at the rotor exit. As mentioned in the previous section, the measured difference in effective flow area varied by up to 3.3% depending on the inlet profile.

A calculation can be done to ensure that the observed change in effective area was responsible for the calculated change in the total-to-static pressure rise coefficient near stall. By combining the calculated change in exit effective flow area with the equations

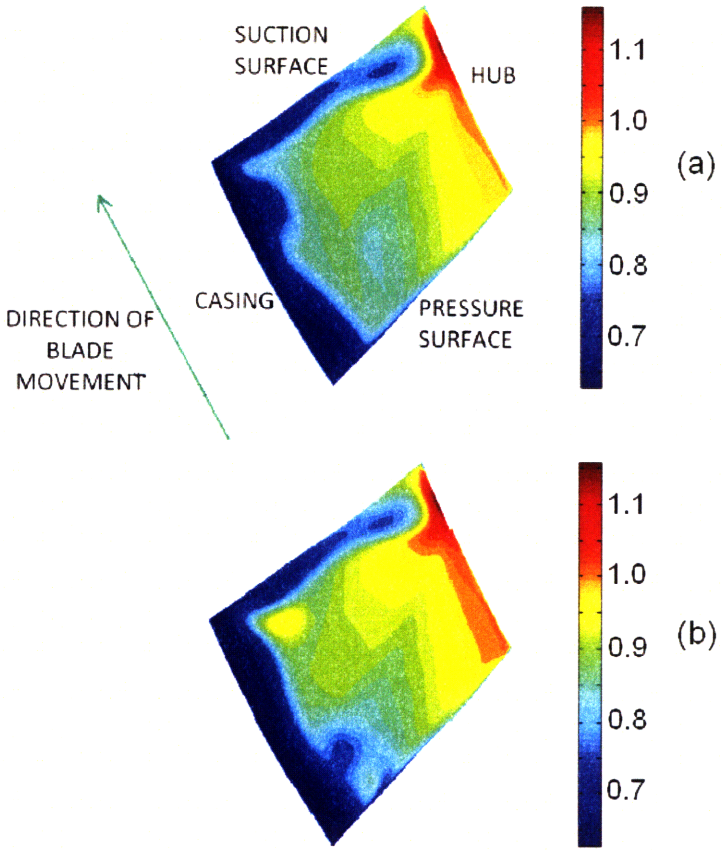

Figure 6.5: Relative stagnation pressure contours at the rotor exit of the (a) uniform inlet case and (b) the stratified inlet postion 1. The tip clearance-related blockage is clearly visible as the region of low relative stagnation pressure fluid on the casing.

describing compressible flow in a diffuser, the resultant change in rotor exit pressure (p_2) can be estimated.

Based on the exit relative Mach number and variation in effective flow area for the stratification cases, the variation in static pressure rise at the rotor exit should be approximately 1.1%. Assuming the rotor inlet stagnation pressure, inlet static pressure, and inlet dynamic pressure are unchanged, the change in exit static pressure rise can then be used to determine the change in inlet total-to-static pressure ratio through equation 6.5.

$$\Delta C_{p,t-s} \approx \frac{\Delta p_2}{q_1'} \tag{6.5}$$

It is estimated that the change in total-to-static pressure rise coefficient from the measured change in blockage is 0.068. The actual variation in total-to-static pressure coefficient from the three-dimensional numerical calculations is 0.031. The approximate calculation overestimates the change in $C_{p,t-s}$ due to change in stratification, but is of the same magnitude, showing that the change in blockage could be the cause of the performance changes observed.

In terms of three-dimensional effects, one can also apply the procedure described in section 4.1 to attain a more beneficial phasing near the casing. Instead of changing the B_3 parameter to place the high time-mean relative stagnation pressure on the suction surface, B_3 should be altered such that high stagnation fluid forms the core of the tip clearance vortex.

6.5 Summary

If phase-locked vortex shedding is significant near the casing, it may be possible to choose the wake phase to increase the relative stagnation pressure within the vortex core. The result would be a greater maximum pressure rise, and possibly a larger stable flow range. A three-dimensional numerical experiment was run as a plausibility test to show that the idea is worth further pursuit. In the numerical experiments, the total-to-static pressure rise coefficient for the rotor passage at near stall conditions varied by 0.031, depending on the relative stagnation pressure profile at the rotor inlet.

Chapter 7

Summary and Conclusions

7.1 Summary

A transonic rotor has been examined computationally and analytically to determine how the path of wake vortices from an upstream vane affects the performance of a downstream rotor. In a situation in which the shedding of the wake vortices is phase-locked to the rotor position, there is a corresponding time-mean effect on the performance of the rotor. Analysis of the flowfield from unsteady three-dimensional calculations of the SMI geometry was used to justify the use of two-dimensional unsteady numerical experiments to assess the impact of wake phase on performance. Appropriate analysis of the two-dimensional unsteady calculations, in turn, revealed that the effects of the phase-locked wake vortices could be explained using a steady two-dimensional calculation. Thus, steady two-dimensional numerical experiments were used to identify the underlying fluid mechanisms that caused the dependence of compressor performance on wake phasing, and a parametric study of these steady two-dimensional calculations was performed to show the scaling of the wake phasing effects with flow parameters.

The three-dimensional effects of wake phasing on the tip clearance flow were also investigated. A steady three-dimensional model was employed to estimate the influence of the phase-locked vortices on the tip clearance flow and thus the peak pressure rise capability and stability, and to reveal the basic mechanisms behind the influence of wake phasing on the casing endwall flow.

In finding a mechanistic explanation for the impact of the wake phasing on the performance of a highly-loaded high Mach number compressor, one of the reasons for the qualitatively different performance of HLHM compressors compared to low speed ma-

chines has been quantified. The modeling techniques introduced in this thesis can thus be used to improve design methodology for advanced HLHM compressors.

7.2 Conclusions

The main conclusions of the research are as follows:

- A change in the upstream wake phase impacts the work input of a downstream rotor. For the configurations investigated the change in rotor work input was 3%.
- A steady model that explains the work input changes with wake phase is described. The time-mean relative stagnation pressure of the fluid adjacent to the blade is dependent on the wake phase. If the high relative stagnation pressure fluid is adjacent to the rotor, the edge velocity of the boundary layer is larger than if low relative stagnation pressure fluid is adjacent to the blade. The higher boundary layer edge velocity results in a smaller rotor boundary layer displacement thickness and less flow deviation, and therefore greater diffusion capability.
- The scaling between the effects of wake phasing and flow parameters such as relative Mach number and magnitude of the time-mean relative stagnation pressure nonuniformity at the rotor inlet have been quantified. The effect of compressibility scales as a Prandtl-Glauert transformation. The impact on work input is proportional to the magnitude of the relative stagnation pressure nonuniformity, to a good approximation.
- The amplitude of the time-mean relative stagnation pressure nonuniformity, associated with wake phasing, scales approximately linearly with the ratio of vane trailing edge thickness to vane pitch.
- The amplitude of the time-mean relative stagnation pressure nonuniformity is roughly independent of the loading on the upstream vane row. The DPT obtained in the deswirler-rotor configuration was small, regardless of the loading on the deswirler.

- Model calculations show that the tip clearance vortex core, and consequently the compressor peak pressure rise and flowrange, can be beneficially affected by changes in wake phase near the casing. Changes in wake phasing affect the relative stagnation pressure of the tip clearance vortex, which affects the magnitude of tip clearance-related blockage at the rotor exit.

- Guidelines for optimizing the wake phase at a given span to enhance the performance of highly-loaded, high Mach number compressors are given. To achieve greater work input through the rotor, the wake phasing should be chosen so the time-mean relative stagnation pressure is greatest in the region adjacent to the rotor suction surface. The B_3 parameter can be used to determine how the compressor geometry should be altered to achieve the desired wake phase.

Chapter 8

Future Work

1. A survey of two-dimensional and three-dimensional compressor geometries should be done, with particular attention being paid to the flow features that may be indicative of the wake phasing phenomenon. The purpose of this study should be to determine to what extent the wake phasing might be important in a typical compressor geometry.

   The results shown in this paper indicate that the effect may not be large, since the trailing edges of most compressor blades are thin. However, the inter-bladerow spacing used to obtain these results was large compared to actual geometry. As explained earlier, this large baseline inter-bladerow spacing was necessary in order for the numerical experiments to adequately isolate the effects of the wake phasing. Now, armed with an understanding of the wake phasing, the flowfield of a closely spaced vane-rotor combination needs to be examined to determine more precisely how important the wake phasing phenomenon might be for a typical high Mach number, highly-loaded compressor, with small inter-bladerow spacings.

   Put differently, the relationship between the time-mean relative stagnation pressure profile magnitude and the vane trailing edge thickness is known; but we would also like to know the relationship between the time-mean relative stagnation pressure profile magnitude and the inter-bladerow spacing. The relationship is likely monotonic, with closer spacings resulting in larger nonuniformity, but the sensitivity of the time-mean relative stagnation pressure profile amplitude to the interblade row spacing is yet to be quantified.

2. The investigation of wake phasing in turbine stages would also be worthwhile. Tur-

bine blades are generally thicker than compressor blades, so the findings of this thesis may be pertinent to the performance of turbine bladerows and it may therefore be possible to increase the work that is extracted from a turbine stage through deliberate choice of the wake phase. The performance of low pressure turbines is especially affected by changes in operational conditions, such as a reduction in Reynolds number due to an increase in cruise altitude. An investigation of the wake phasing phenomenon in such geometries may yield a solution that allows the reduction in work extraction with operational changes to be mitigated.

3. A final topic that may be worth further pursuit is a closer examination of the relationship between wake phase and the stage efficiency. This topic was touched on briefly in this thesis, and some of the approximate trends of efficiency vs. wake phase were examined. However, a closer examination should be done in order to more precisely understand how phasing affects efficiency, and elucidate the relevant scaling. There is an apparent discrepancy between the results shown in this thesis and those of Zachcial and Nuernberger [15]; the phase which resulted in the greatest efficiency in [15] is approximately 180 degrees different than the phase that resulted in greatest efficiency in the current research. However, the wake phase that results in the highest efficiency may change depending on the loading of the blades. The topic is described in further detail in Appendix B.

Bibliography

[1] Kerrebrock, J., 1992. *Aircraft Engines and Gas Turbines, Second Edition.* The MIT Press, Cambridge, MA.

[2] Cumpsty, N., 2004. *Compressor Aerodynamics, Second Edition.* Krieger Publishing Company, Melbourne, FL.

[3] Ottavy, X., Trebinjac, I., and Vouillarmet, A., 2001. "Analysis of the Interrow Flowfield Within a Transonic Axial Compressor: Part 1 - Experimental Investigation". *ASME Journal of Turbomachinery,* **123** , pp. 49–56.

[4] Ottavy, X., Trebinjac, I., and Vouillarmet, A., 2001. "Analysis of the Interrow Flowfield Within a Transonic Axial Compressor: Part 2 - Unsteady Flow Analysis". *ASME Journal of Turbomachinery,* **123** , pp. 57–63.

[5] Gorrell, S., Okiishi, T., and Copenhaver, W., 2003. "Stator-Rotor Interactions in a Transonic Compressor: Part 1 - Effect of Blade-Row Spacing On Performance". *ASME Journal of Turbomachinery,* **125** .

[6] Gorrell, S., Car, D., Puterbaugh, S., Estevadeordal, J., and Okiishi, T., 2006. "An Investigation of Wake-Shock Interactions in a Transonic Compressor with DPIV and Time-Accurate CFD". *ASME Journal of Turbomachinery,* **128** , pp. 616–626.

[7] Smith, L., 1970. "Casing Boundary Layers in Multistage Axial Flow Compressors". *Flow Research on Blading* .

[8] Hetherington, R., and Moritz, R. R., 1975. "The Influence of Unsteady Flow Phenomena on the Design and Operation of Aero Engines". *Unsteady Phenomena in Turbomachines* . AGARD CP-177, North Atlantic Treaty Organization.

[9] Mikolajczak, A. A., 1975. "The Practical Importance of Unsteady Flow". *Unsteady Phenomena in Turbomachines* . AGARD CP-177.

[10] Smith, L., 1966. "Wake Dispersion in Turbomachines". *ASME Journal of Basic Engineering,* **88** , pp. 688–690.

[11] Adamczyk, J. J., 1996. "Wake Mixing in Axial Flow Compressors". *ASME 96-GT-29* .

[12] Greitzer, E., Tan, C., and Graf, M., 2004. *Internal Flow: Concepts and Applications.* Cambridge University Press, Cambridge, UK.

[13] Valkov, T., and Tan, C., 1999. "Effects of Upstream Rotor Vortical Disturbances on Time-Average Performance of Axial Compressor Stator: Part 1- Framework of Technical Approach and Rotor Wakes-Stator Blade Interaction, and Part 2- Rotor Tip Leakage and Discrete Streamwise Vortex -Stator Blade Interaction". *ASME Journal of Turbomachinery,* **121, no.3** .

[14] Botros, B., 2008. Impact of Unsteady Flow Processes on the Performance of a High Speed Axial Flow Compressor. Master's thesis, Massachusetts Institute of Technology, Cambridge, Massachusetts. Dept. of Mechanical Engineering.

[15] Zachcial, A., and Nuernberger, D., 2003. "A Numerical Study on the Influence of Vane-Blade Spacing on a Compressor Stage and Sub- and Transonic Operating Conditions". *ASME GT2003-38020* .

[16] Chen, J., 2001. "A Parallel Flow Solver for Unsteady Multiple Blade Row Turbomachinery Simulations". *ASME GT2001-0348* .

[17] Zante, D. V., Chen, J., Hathaway, M., and Chriss, R. "The Influence of Compressor Blade Row Interaction Modeling on Performance Estimates From Time-Accurate, Multistage, Navier-Stokes Simulations". *ASME Journal of Turbomachinery.*

[18] Villanueva, A. D., 2006. Characterization of the flow field response to vaneless space reduction in centrifugal compressors. Master's thesis, Massachusetts Institute of Technology, Cambridge, Massachusetts. Dept. of Aeronautics and Astronautics.

[19] Wolf, S., and Johnston, J., 1966. Effects of Nonuniform Inlet Velocity Profiles on Flow Regimes and Performance in Two-Dimensional Diffusers. Tech. Rep. Report PD-12, Stanford, CA.

[20] Wolf, S., and Johnston, J., 1969. "Effects of Nonuniform Inlet Velocity Profiles on Flow Regimes and Performance in Two-Dimensional Diffusers". *ASME Journal of Basic Engineering,* **91** , pp. 462–474.

[21] Key, N., Lawless, P., and Fleeter, S., 2008. "An Investigation of the Flow Physics of Vane Clocking Using Unsteady Flow Measurements". *ASME GT2008-51091* .

[22] Greitzer, E., Paterson, R., and Tan, C., 1985. "An Approximate Substitution Principle for Viscous Heat Conducting Flows". *Proc. Roy. Soc. London,* **401** , pp. 163–193.

[23] Drela, M., and Youngren, H., 1998. A User's Guide to MISES 2.53. Tech. rep.

[24] Schreiber, H., and Frost, G., 1984. "Experimental Investigation of a Transonic Compressor Rotor Blade Section". pp. 288–294.

[25] List, M., Gorrell, S., and Turner, M., 2008. "Investigation of Loss Generation in an Embedded Transonic Fan Stage at Several Gaps Usings High Fidelity, Time-Accurate CFD". *ASME GT2008-51220* .

[26] Khalid, S., Khalsa, A., Waitz, I., Tan, C., Greitzer, E., Cumpsty, N., Adamczyk, J., and Marble, F., 1999. "Endwall Blockage in Axial Compressors". *ASME Journal of Turbomachinery,* **121** , pp. 499–509.

[27] Thompson, D., King, P., and Rabe, D., 1998. "Experimental Investigation of Stepped Tip Gap Effects on the Performance of a Transonic Axial-Flow Compressor Rotor". *ASME Journal of Turbomachinery,* **120** .

[28] Murray, N. P. Effects of Impeller-Diffuser Interaction on Centrifugal Compressor Performance.

[29] Barankiewicz, W. S., and Hathaway, M. D., 1997. "Effects of Stator Indexing on Performance in a Low Speed Multistage Axial Compressor".

Appendix A

Link Between Diffusion and Blade Force

In this appendix, we present an approximate control volume analysis that links the results from the diffuser experiments of Wolf and Johnston [19, 20] to the two-dimensional compressor calculations from Chapters 3, 4, and 5. Specifically, we show that estimates of the reduction in diffusion capability of the rotor, based on the diffuser results, are in rough accord with the observed reduction in rotor circumferential force.

The control volume examined is shown in Figure A.1. The flow is taken as incompressible and two-dimensional. Station 1 is at the entrance to the rotor passage and station 2 is at the exit of the rotor passage. All quantities pertaining to this analysis are measured in the rotor relative frame.

Two effects decrease the effective flow area at the blade row exit: deviation of the flow and blockage due to boundary layer displacement thickness. For simplicity we examine these effects separately. As in Figure A.2, we refer to the situation in which the deviation at the exit is significant in changing the effective flow area, but the blockage is insignificant, as "Case 1" and to the situation in which the deviation at the exit is insignificant, but the blockage is significant, as "Case 2". In both these cases, it will be shown that the reduction in pressure rise results in a smaller circumferential blade force.

The circumferential blade force component is equal to the net change in circumferential momentum flux across the blade row. The ratio of exit to inlet circumferential momentum is given in Equation (A.1), which, using continuity, can be expressed as,

$$\frac{\rho u_{x,2} u_{y,2} W_2}{\rho u_{x,1} u_{y,1} W_1} = \frac{u_{y,2}}{u_{y,1}} = \frac{|\mathbf{u}_2| \, sin\beta_2}{|\mathbf{u}_1| \, sin\beta_1}. \tag{A.1}$$

The circumferential blade force per unit flow area normalized by the inlet flux of circumferential momentum per unit flow area is thus,

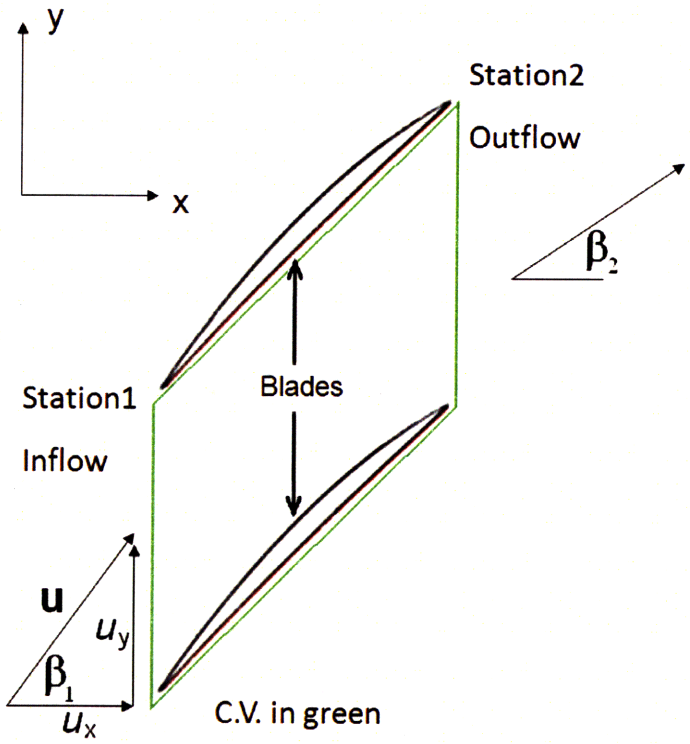

Figure A.1: Control volume used in analysis of rotor circumferential force. All velocity vectors in this analysis are considered relative to the rotor.

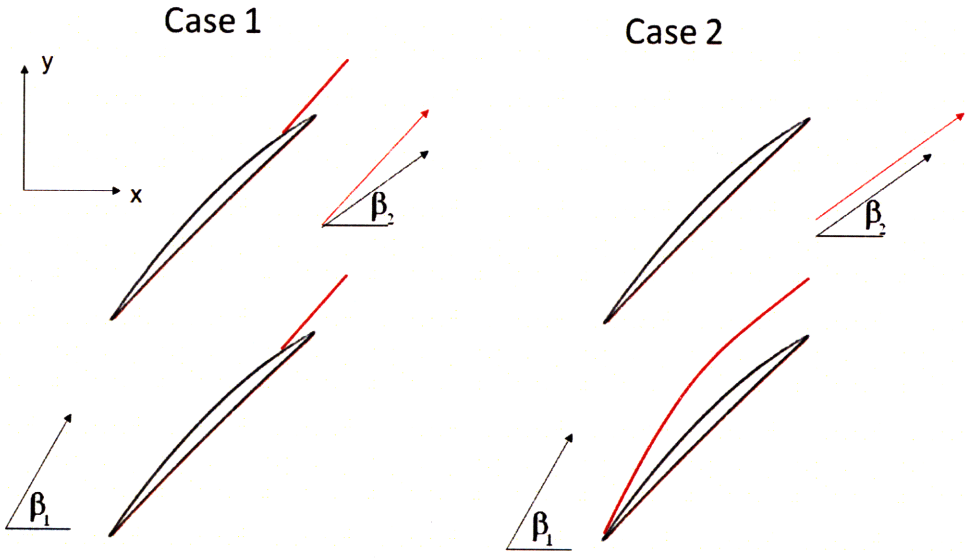

Figure A.2: Decrease in exit area in a blade passage. The red line represents the edge of the suction side boundary layer. In Case 1, deviation at the rotor exit causes the rotor exit velocity to change from the black arrow (no deviation) to the red arrow. In Case 2, the boundary layer blockage causes the change from an ideal situation with no blockage.

$$\frac{F_\theta}{\rho u_{x,1} u_{y,1}} = 1 - \frac{|\mathbf{u}_2| \, sin\beta_2}{|\mathbf{u}_1| \, sin\beta_1}. \tag{A.2}$$

From Bernoulli's equation we can write $|\mathbf{u}_2| / |\mathbf{u}_1|$ in terms of the static pressure rise coefficient. Combining this fact with Eqn. A.2 yields,

$$\frac{F_\theta}{\rho u_{x,1} u_{y,1}} = 1 - (1 - C_p)^{0.5} \frac{sin\beta_2}{sin\beta_1}. \tag{A.3}$$

For Case 1, an increase in the deviation angle increases β_2 and decreases C_p, both of which, as in Eqn. A.3, decrease the circumferential force component. For Case 2, an increase in blockage with negligible deviation, there is an effect only on C_p only, but, again, a decrease in the circumferential blade force.

Using the scaling for relative stagnation pressure nonuniformity from the compressor simulations, the results of Wolf and Johnston can be used to estimate the variation in static pressure rise coefficient that would accompany a phase change of the relative stagnation pressure profile at the inlet, and hence the change in circumferential force. The comparison is made at the appropriate aspect ratio (diffuser length divided by the normal flow area at the diffuser inlet). For the data shown in Figure 3.7, the aspect ratio was 3, which is close to the aspect ratio of 2.7 for the two-dimensional compressor geometry. The ratio of $\cos\beta_2$ to $\cos\beta_1$ yields the appropriate area ratio that corresponds to the compressor geometry. For the compressor geometry, the area ratio (ratio of exit effective flow area to inlet effective flow area) is 1.33, which is below the range at which there is data comparing the results of the Wake and Jet profiles from the Wolf and Johnston experiments. Therefore, the difference in static pressure rise predicted by the data set was determined through the use of interpolation. An assumption was made that at an area ratio of 1, the difference in pressure rise coefficient would be 0, and that between an area ratio of 1 and 1.5, the difference in static pressure rise coefficient (between the "High Velocity on Walls" and "Low Velocity on Walls" cases depicted in Figure 3.6) is linearly dependent on the area ratio.

Further assumptions include that the "High Velocity on Walls" profile results in the greatest pressure rise, while the "Low Velocity on Walls" profile corresponds to the lowest pressure rise. Based on the results from the MSUTurbo and the MISES calculations, this is a good assumption. We have also assumed that the drop in mass-averaged relative stagnation pressure across the passage is much smaller (an order of magnitude or less) than the inlet dynamic pressure, and that the boundary displacement thickness is much smaller than the rotor pitch. Lastly, it was assumed that the minor differences in the actual shape of the relative stagnation profile between the Wolf and Johnston profile and the profile used in the MISES calculation presented in this paper is not cause for a large discrepancy.

For Case 1 (deviation) the change in circumferential force due to change in position of the inlet profile is estimated to be 5.6%. For Case 2 (blockage) the estimated variation in circumferential force is 3.0%. In the numerical simulations there is a combination of flow deviation and blockage, but the latter is dominant, so one could expect the variation to fall within the range of 3-6%. The MISES calculations carried out (described in Section 4.1) did in fact show roughly 4% variation in circumferential blade force, depending on the position of the inlet profile. Although several approximations were made in this analysis, the estimate is accurate enough to show that the difference in diffusion capability is linked directly to the change in circumferential blade force.

Appendix B

Possible Explanation for Efficiency Trends

The focus of this research is on the effect wake phasing from an upstream vane has on the work input of a downstream rotor, and only a cursory examination of the resultant changes in efficiency was done. This appendix will briefly compare the efficiency trends for the numerical experiments described in this research to those results from the relevant literature.

For the unsteady simulations in Chapter 3, as well as the steady simulations in Chapters 3, 4, and 5, the wake phase which optimized rotor work input was approximately equal to the phase that maximized the efficiency. The rotor boundary layer remained attached and had a reduced displacement thickness when the high relative stagnation pressure fluid was on the blade surface, resulting in greater diffusion capability and reduced mixing losses downstream of the rotor, compared to when the low relative stagnation pressure fluid bathed the blade. This trend of efficiency vs. wake phase is opposite to that calculated by Zachcial and Nuernberger, who measured a greater efficiency when the wake vortices were placed such that the boundary layer edge velocity was reduced.

The effect of changes in wake phase is also similar to the effect of changes in clocking. The research on clocking done by Key, et. al. [21] can be used to explain the apparent discrepancy in efficiency trends. Key found that for a highly-loaded compressor stage, the efficiency was greatest when the wake shed upstream stator passed through the midpitch of the downstream stator, and that the variation in efficiency due to clocking was 1.08 points. At a lower loading, however, the trend in efficiency with vane clocking was opposite to the highly-loaded results, with a variation in efficiency of 0.27 points. In other words, the highly-loaded results were consistent with the calculations presented in this thesis, while the lowly-loaded results were consistent with the calculations of

Zachcial and Nuernberger. Thus, it is possible that if the loading on the blade geometry tested by Zachcial and Nuernberger were increased, the trend of efficiency versus vortex position would be reversed

According to Key, the reason for the change is that the key mechanism by which the upstream wake affects the boundary layer of the downstream stator changes with loading [21]. Physical experiments performed by Barankiewicz, et al. corroborate this conclusion [29]. At low loading, when the low stagnation pressure fluid within the wake from the upstream stator impinges on the leading edge of the downstream stator, the fluctuation in incidence angle resulting from the unsteady passing of the rotor row (between the stator rows) is mitigated, thus reducing the time-averaged loss incurred and increasing efficiency. At high loading, the impingement of the low stagnation pressure fluid on the leading edge of the downstream stator causes the suction side bounday layer to separate and therefore reduces the efficiency. Measurements and associated calculations of losses due to mixing of the rotor wake made by Botros [14] confirm the trend of wake phase and efficiency for the highly-loaded case.

Appendix C

Modifications made to MISES code

Prof. Mark Drela (the creator of MISES) was consulted to determine how the scaling experiments described in section 5.1 could be performed using MISES. To allow for the specification of the nonuniform inlet stagnation pressure profile, the code was changed in the following manner. Firstly, the following section of code was inserted at line 117 of src/ises/setup.f:

```
      PSI(1) = 0.0
      DO j=2,JJ
         PSI(j) = PSI(j-1)+MFRACT(j-1)
      ENDDO

      DO j=1,JJ-1
         PSIH = 0.5*(PSI(j)+PSI(j+1))
C The following line allows easy pitchwise shifting of profile
         PSIE = PSIH + 0

C The following line ensures that the pitchwise position remains
C between 0 and 1
         IF (PSIE .GT. 1) THEN
            PSIE = PSIE-1
         ENDIF

C The hyperbolic tangent profiles are set up by the following six
C lines.  The amplitude of the profile is altered by changing the
C constant which the TanH is multiplied to.

         IF (PSIE .LE. 0.5) THEN
         PSTJ(j) = PSTRO*(1+0.05*TanH(4*3.14159*PSIE-3.14159))
         ENDIF

         IF (PSIE .GT. 0.5) THEN
         PSTJ(j) = PSTRO*(1-0.05*TanH(4*3.14159*PSIE-3*3.14159))
         ENDIF


      ENDDO
```

The pitchwise position of the inlet stagnation pressure profile can be changed by altering the difference PSIE and PSIH in the code above, and the magnitude and shape of the

inlet stagnation pressure profile can be changed by altering the definition for PSTJ. Also, line 438 is changed to the following code:

```
REZ    = PST1 - PSTJ(JO)
```

Finally, the src/ises/update.f file is altered by placing the following segment of code at line 917:

```
 CALL MIXOUT(XINL,QXINLZ    ,QYINLZ    ,RHOINLZ    ,PINLZ    ,
&                  QXOUT_GL,QYOUT_GL,RHOOUT_GL,POUT_GL )
 QINLZ = SQRT(QXINLZ**2+QYINLZ**2)
 MINLZ = QINLZ * SQRT(RHOINLZ/(GAM*PINLZ))
 SINLZ = QYINLZ/QXINLZ
```

The changes made to the update.f file cause the constant area mixed-out inlet slope (which is the tangent of the flow angle) to be displayed along with the convergence data after each iteration. The slope is displayed in place of the "dSin1" data. The flow angle is important in ensuring that the flow coefficient at which the data sets are compared are the same. The alternate source code must be recompiled in order for the changes to take effect.